Semiconductor Radiation Detectors

16

Douglas S. McGregor

Contents

D. S. McGregor (✉)
Semiconductor Materials and Radiological Technologies Laboratory, Mechanical and Nuclear Engineering, Kansas State University, Manhattan, KS, USA
e-mail: mcgregor@ksu.edu

I. Fleck et al. (eds.), *Handbook of Particle Detection and Imaging*,
https://doi.org/10.1007/978-3-319-93785-4_16

Abstract

The basic principles for the design and operation of semiconductor detectors are presented. A summary treatment of *pn* junction and Schottky junction formation is described. Common semiconductor configurations are discussed, including planar and coaxial detectors for γ-ray spectroscopy and various detectors for α-particle spectroscopy.

Nomenclature

A	detector contact area
C_{det}	detector capacitance
C_{tot}	total coupling capacitance
E	energy of radiation quantum
E_A	acceptor energy
E_C	conduction band edge
E_D	donor energy
E_F	Fermi energy
E_V	valence band edge
ϵ_s	semiconductor permittivity
ϵ_0	free space permittivity
$FWHM$	full width at half maximum
μ_e	electron mobility
μ_h	hole mobility
μ_s	majority carrier mobility
N_A	acceptor concentration
N_A^-	ionized acceptor concentration
N_D	donor concentration
N_D^+	ionized donor concentration
N_s	majority impurity concentration
n_i	intrinsic concentration
ξ_e	electron extraction factor
ξ_h	hole extraction factor
n	electron concentration
p	hole concentration
q	electron charge
ΔQ	charge collected from detector
Q	charge excited in detector
ρ_c	space charge density
ρ_s	semiconductor resistivity
τ_e	electron lifetime
τ_h	hole lifetime
ϕ_m	metal work function
ϕ_s	semiconductor work function
ϕ_b	barrier potential
V	applied detector voltage

V_{bi}	built-in detector potential
v_e	electron velocity
v_h	hole velocity
V_{in}	detector input voltage signal
V_w	weighting potential
W	detector active region width
w	average ionization energy
χ_s	semiconductor electron affinity
ψ	potential
Z	atomic number

Introduction

Semiconductors are far more desirable for energy spectroscopy than gas-filled detectors or scintillation detectors because they are capable of much higher-energy resolution. The observed improvement is largely due to the better statistics regarding the number of signal carriers (charges) excited by a radiation interaction. On average, it only takes 3 to 5 eV to produce an electron-hole pair in a semiconductor. By comparison, it takes between 25 and 40 eV to produce an electron-ion pair in a gas-filled detector and between 100 eV and 1 keV to produce a single photoelectron ejection from the photomultiplier tube (PMT) photocathode in a scintillation/PMT detector (primarily due to light reflections and poor quantum efficiency at the photocathode). Hence, a semiconductor produces more charge carriers from the primary ionization event and thus reduces the statistical fluctuation in the energy resolution.

Semiconductor radiation detectors have many different shapes, sizes, and configurations, yet there are some basic designs that, in some form or another, can be attributed to practically all semiconductor radiation detectors. These basic designs include *pn* junction diodes, *pin* junction diodes, Schottky diodes, resistive detectors, and photoconductors. The vast field of semiconductor radiation detectors is much too large to describe in a single book chapter. As a result, only those concepts needed to understand basic detector operations and characteristics are offered here. Much of the material presented here is extracted from a more detailed description in McGregor and Shultis (2021). A selected list of literature is included at the end of the chapter that offers more information on various semiconductor detector configurations, characterizations, and operations. Example performances of some commercial detectors are listed.

Definitions

In the following section are listed and described certain basic definitions and concepts used in discussions of semiconductor detectors. For a more detailed discussion regarding these concepts, the reader is directed to the reference literature at the chapter end.

Energy Band Gap

In free space, a single atom has quantized and discrete allowed energy states. The Pauli exclusion principle states that no two electrons can occupy the same four quantum numbers (n, l, m_l, m_s), where n is the principle number referring to energy, l is the angular momentum quantum number, m_l is the magnetic quantum number, and m_s is the spin. However, a solid material, such as a semiconductor crystal, is a matrix of atoms arranged in a lattice such that the various potentials of each of the atoms affect the surrounding neighbors and those electrons associated with them. If two atoms are forced into close proximity, each initially with identical quantum numbers, then something must change such that the exclusion principle is not violated, which is satisfied by the appearance of degenerate energy states. In other words, the original energy levels split such that two states appear where there was only one before (Fig. 1).

Consider the issue of a solid, where typical atomic densities range from 10^{21} to 10^{23} atoms cm^{-3}. The total number of energy states must also split to accommodate

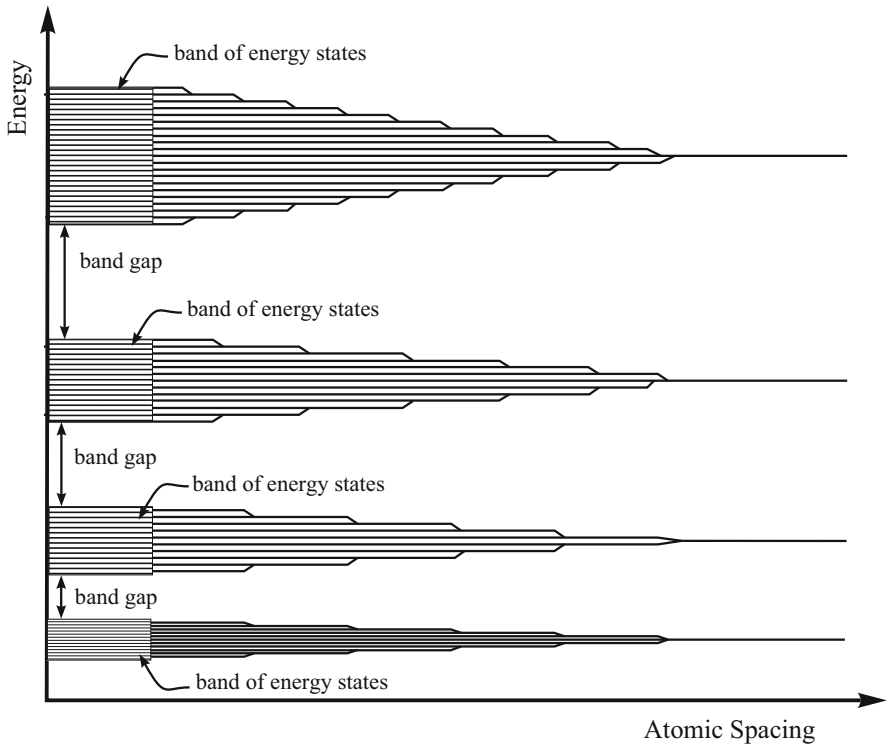

Fig. 1 As atoms are brought closer together, their allowed energy states split into degenerate states. In a solid medium, the high atomic density causes these degenerate states to form quasi-continua referred to as energy bands

the electron density, which form bands of states in place of what were once individual states for a single atom (Fig. 1). These bands may overlap, may be relatively close to each other in energy with a small energy gap between them, or may form with large energy gaps between the bands (Fig. 2). Electrons in the bands behave almost as though they are in an energy continuum, but it is actually a *quasi-continuum*, in which there is a defined density of available states in each of the bands. The density of states is still predetermined by the original total number of states of the individual atoms.

Each of these energy bands has a certain density of allowed energy states that can be occupied by an electron. The electrical conductivity of a solid is determined by many parameters, which include charge carrier mobility, the density of free charge carriers available in a partially filled energy band, and the availability of unfilled energy states in the partially filled band. As conceptual examples, shown in Fig. 2 are examples of simplistic band diagrams for (a) insulators, (b) conductors, and (c) semiconductors. In Fig. 2a, the *valence band*, which is active in chemical binding of electrons in compounds, is filled, and the next available energy band is devoid of electrons. In typical notation, the upper energy limit of the valence band is denoted E_V, and the lower-energy limit of the *conduction band* is denoted E_C. The energy difference between E_C and E_V is a forbidden energy region, referred to as the energy band gap and denoted E_g. If the band gap energy is large such that electrons are not thermally excited from the valence band into the conduction band, the material is considered an insulator. Conduction can only take place provided that there are empty states for charge carriers to occupy in lateral energy space. Because the valence band is completely full of charge carriers, there are no empty states, hence no conduction. Further, the conduction band has empty states but no charge carriers; hence again conduction does not take place.

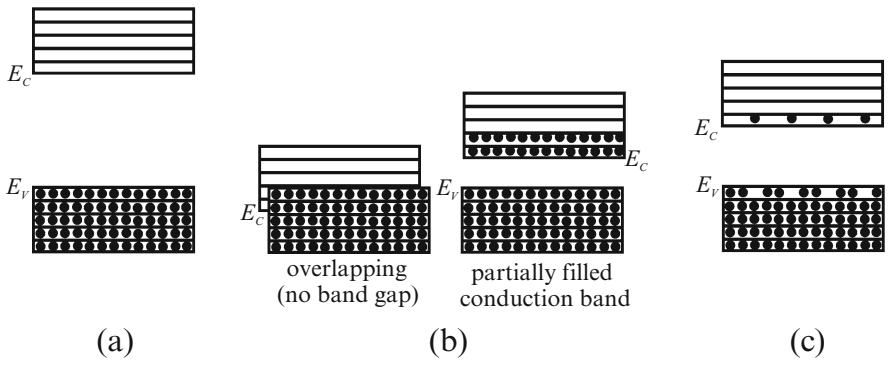

Fig. 2 Shown are depictions of simple band diagrams for (**a**) insulators, (**b**) conductors, and (**c**) semiconductors. In (**b**) there are two depictions for conductors, one in which a filled valence band overlaps the conduction band and the other in which the valence band is full with a partially filled conduction band

In Fig. 2b, there are two examples of conductors. In the first example, the valence band and the conduction band overlap such that electrons can easily move from the filled valence band into the partially filled conduction band without a change of energy. Hence, there are plenty of unfilled states with an overlapping reservoir of electrons (the valence band) that can move to the conduction band, thereby giving rise to free conduction. In the other example, the valence band is filled, and the conduction band is partially filled with a high density of electrons, even at low temperature. Again the conditions exist for free conduction.

In Fig. 2c, there is a band gap similar to the insulator example, except the band gap is relatively small. As a result, some electrons are thermally excited from the valence band into the conduction band where they can freely conduct. However, the density of the electrons in the conduction band is determined largely by the band gap energy and the temperature. At low enough temperature, the electrons will all return to the valence band, and the material will behave as an insulator. As the temperature is increased, more and more electrons will cross the band gap into the conduction band, and the material conductivity will continue to increase. Often this class of materials is separated into *semiconductors* and *semi-insulators*, roughly defined by the band gap energy. Typically, band gap energies ranging up to approximately 1.4 eV constitute a class of materials commonly designated as semiconductors, while band gap energies ranging from 1.4 eV up to 5 eV are considered semi-insulators. Band gaps exceeding 5 eV form the insulator class of materials. However, these ranges are not rigidly classified, and often semi-insulators and semiconductors are treated as the same, which will be the case in this chapter.

Charge Carrier Concentration

The probability distribution of electrons with energy E_e is determined by Fermi-Dirac statistics,

$$F(E) = \frac{1}{1 + \exp\left[\dfrac{E_e - E_F}{kT}\right]}, \tag{1}$$

where k is Boltzmann's constant (see Table 1), T is the absolute temperature, and E_F is the Fermi energy level (Sze 1981). The Fermi energy is the energy level, at 0 K temperature, where all states below it are filled and all above it are empty. Equation (1) can be used to determine the density of electrons in the conduction band, with knowledge that electrons will not be present in the band gap; hence Eq. (1) is valid for $E_e \geq E_C$ and $E_e \leq E_V$. From Eq. (1), the probability that an electron crosses the band gap to the conduction band will increase with increasing temperature, which should be intuitively obvious.

The concentration of electrons in the conduction band is denoted n, and the concentration of empty states in the valence band is denoted p. These empty

states are treated as positive charge carriers called "holes," which greatly simplifies calculations. For a pure material, the electrons in the conduction band arrive at the expense of leaving an equal density of holes in the valence band. Hence, $n = p$, which is referred to as the intrinsic case. Typically, the intrinsic concentration of both electrons and holes is denoted n_i. It can be shown that,

$$n = \int_{E_C}^{\infty} N(E)F(E)dE \approx N_C \exp\left(-\frac{E_C - E_F}{kT}\right), \tag{2}$$

where $N(E)$ is the function describing the allowed density of states and N_C is the effective density of allowed states in the conduction band. Similarly, describing the unfilled states or holes in the valence band,

$$p = \int_{-\infty}^{E_V} N(E)[1 - F(E)]dE \approx N_V \exp\left(-\frac{E_F - E_V}{kT}\right), \tag{3}$$

where N_V is the effective density of allowed states in the valence band (Sze 1981).

Dopant Impurities

Dopant impurities are often added to a semiconductor to control the electrical properties. Dopants that add excess electrons to the chemical binding are called donors, because they need only a slight amount of energy to liberate these excess electrons into the conduction band. Dopants that lack an electron to complete the valence bonding are called acceptors, because they need only a slight amount of energy to accept electrons from the valence band into their unfilled states. The simplified energy band structures for intrinsic, n-type, and p-type materials are depicted in Fig. 3. The concentration of donor atoms is denoted N_D with energy level E_D, and the concentration of acceptor atoms is denoted N_A with energy level E_A. If donors are added to the semiconductor, then the concentration of holes is reduced. The opposite condition is achieved if acceptors are added to the semiconductor. The general relationship between the free electron concentration and the free hole concentration is

$$np = n_i^2. \tag{4}$$

At room temperature, almost all shallow donors and acceptors are ionized; hence $N_A \approx p$ and $N_D \approx n$. Combining Eqs. (2), (3), and (4), it is easily shown that the intrinsic carrier concentration is

$$n_i = \sqrt{N_C N_V} \exp\left(-\frac{E_g}{2kT}\right). \tag{5}$$

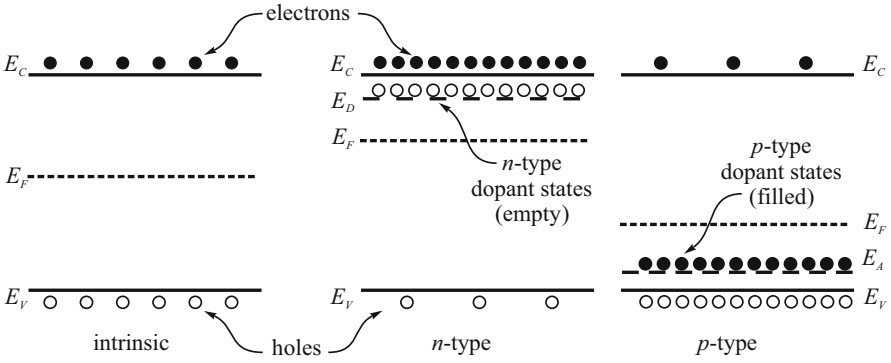

Fig. 3 The simplified energy band structures for intrinsic, n-type, and p-type materials. The electron and hole carrier concentrations are equal for the intrinsic case. Materials doped n-type have an excess of electrons in the conduction band, and materials doped p-type have an excess of holes in the valence band

Equation (5) clearly indicates that the intrinsic charge carrier population n_i decreases with increasing band gap energy E_g and decreasing temperature T.

Carrier Mobility

The motion of a charge carrier can be influenced by diffusion, magnetic fields, and electric fields. The strength of this influence is characterized by the carrier mobility. The valence and conduction bands have different periodic potentials, and for this reason, electron mobility in the conduction band is different than hole mobility in the valence band. Electron mobility is denoted μ_e, and hole mobility is denoted μ_h. The velocity of a charge carrier can be approximated with

$$v_{e,h} = \mu_{e,h}\mathcal{E}, \tag{6}$$

where $\mathcal{E}$ is the electric field magnitude. Equation (6) is a good approximation provided that the electric field is relatively lower than the saturation field (usually below 2×10^3 V cm^{-1}), above which the charge carrier velocities begin to asymptotically approach a saturation limit.

Carrier Lifetime

Charge carriers in the conduction band are dynamically dropping back into the empty states of the valence band, while other electrons gain energy to cross the band gap. Overall, a somewhat constant density of electrons and holes remains in the conduction and valence bands, respectively. The time over which a charge carrier

remains in either band is altered by impurity and defect states that appear in the band gap, which increase the probability of either carrier transferring from either band to an intermediate state or eventually to completion of the recombination process. If a charge carrier falls into a defect state, it is referred to as "trapped," whereas if the charge carrier journey is completed, where an electron falls completely back into a hole in the valence band, it is referred to as having "recombined." The average time period over which an excited electron remains in the conduction band before being trapped or recombining is the electron lifetime, denoted τ_e, and the average time period over which a hole remains in the valence band before being trapped or recombining is the hole lifetime, denoted τ_h.

Material Resistivity

The ability of a semiconductor to conduct electrons is referred to as the material resistivity, with units of Ω·cm. The resistivity of a semiconductor is found with

$$\rho = \frac{1}{q(\mu_e n + \mu_h p)}, \tag{7}$$

where q is the unit electronic charge, μ_e is the electron mobility, and μ_h is the hole mobility. In the case that $n \gg p$, Eq. (7) reduces to

$$\rho \approx \frac{1}{q\mu_e n}, \tag{8}$$

and in the case that $p \gg n$, Eq. (7) reduces to

$$\rho \approx \frac{1}{q\mu_h p}. \tag{9}$$

The resistance of a right parallelepiped block of semiconductor is described by

$$R = \rho \frac{W}{A}, \tag{10}$$

where W is the detector width or length and A is the contact area.

Basic Detector Configurations

Semiconductor detectors can be fashioned into many different device configurations, including junction diodes, Schottky barrier diodes, photoconductors, and photoresistors. To select the most appropriate device configuration, one must consider the semiconductor material and the radiation detection application. Some semiconductor materials are composed of substances that are not easily converted

into junction diodes, such as HgI_2 and PbI_2, whereas other semiconductors, such as Si and Ge, are easily fashioned into junction devices. Some materials, such as GaAs, can be fabricated easily into either photoconductors or Schottky barrier devices, whereas limited doping selection and other chemical constraints prevent some materials from being configured easily as either reverse-biased diodes or photoconductors. These fundamental designs are briefly described in the following sections.

pn Junction

If two blocks of semiconductor material, one doped with N_D donors and the other doped with N_A acceptors, are fused together into contact, then the p-type side of the junction boundary has an excess of free hole charge carriers, and the n-type side of the junction has an excess of free electron charge carriers. The concentration gradient across the junction boundary will cause holes to *diffuse* across the boundary into the n-type side and electrons to *diffuse* over to the p-type side. The free carriers leave behind the immobile host ions, which produce regions of *space charge* of opposite polarity, as depicted in Fig. 4. The result is the production of an internal

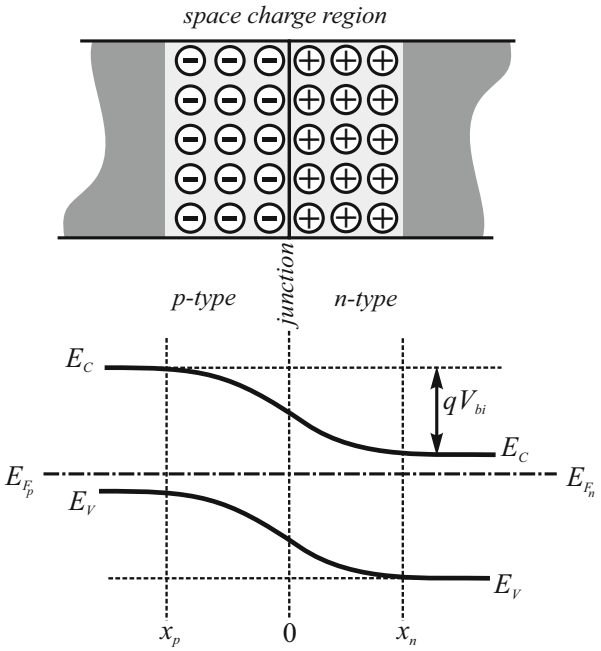

Fig. 4 In the depiction of a *pn* junction at equilibrium, the free charge carriers are swept from the space charge or *depletion* region, leaving behind a polarized zone that produces an internal electric field. Diffusion of charges in one direction is balanced by electric field drift in the other. At equilibrium, the Fermi level is constant across the junction

electric field with an applied force in the opposite direction of the diffusion force. The presence of space charge distorts the band potentials and causes the bands to bend across the junction boundary. The bands continue to distort and bend until the diffusion force is equal to the electric field force, thereby producing a state of equilibrium.

Poisson's equation is used to determine the space charge region width:

$$\frac{\partial^2 \psi}{\partial x^2} = -\frac{\rho_c(x)}{\epsilon_s} = \frac{q}{\epsilon_s}(N_A^- - N_D^+ - p + n), \tag{11}$$

where ρ_c is the volumetric charge density, ϵ_s is the semiconductor permittivity (see Tables 1 and 2), N_D is the dopant density on the n-type side, N_A the dopant density on the p-type side, and n and p are the electron and hole free carrier densities. Under room temperature conditions, the ionized acceptor concentration $N_A^- \approx N_A$, and the ionized donor concentration $N_D^+ \approx N_D$. With the assumption of an abrupt junction and uniform dopant distribution, the depletion width solution is

$$W = \left\{ \frac{2\epsilon_s(V_{bi} - V)}{q} \left(\frac{N_A + N_D}{N_A N_D} \right) \right\}^{1/2}, \tag{12}$$

where V is an externally applied negative voltage and V_{bi} is the built-in potential arising from the energy band bending, as shown in Fig. 4 (Pierret 1989). The value of V_{bi} for common pn junction diodes is approximately 0.7 volts. In the case that one side of the junction is doped much higher than the other side, by at least an order of magnitude, Eq. (12) can be approximated by

$$W \approx \left\{ \frac{2\epsilon_s(V_{bi} - V)}{q N_s} \right\}^{1/2}, \tag{13}$$

Table 1 Some useful physical constants

Constant	Symbol	Magnitude
Avogadro's number	N_0	6.023×10^{23} molecules mol^{-1}
Boltzmann's constant	k	$1.38 \times 10^{-23}\,\text{J K}^{-1} = 8.62 \times 10^{-5}\,\text{eV K}^{-1}$
Electronic charge	q	$1.6 \times 10^{-19}\,\text{C}$
Electron volt	eV	$1.6 \times 10^{-19}\,\text{J}$
Free-electron mass	m	$9.1 \times 10^{-31}\,\text{kg}$
Permittivity of free space	ϵ_0	$8.854 \times 10^{-14}\,\text{F cm}^{-1}$
Permeability of free space	μ_0	$1.257 \times 10^{-8}\,\text{H cm}^{-1}$
Planck's constant	h	$6.625 \times 10^{-34}\,\text{J s}$
Velocity of light	c	$3 \times 10^{10}\,\text{cm s}^{-1}$
Thermal energy at 300 K	kT	0.0259 eV

Table 2 Common semiconductors used as radiation detectors and their properties at 300K

Semiconductor	Atomic number (Z)	Density ($g\,cm^{-3}$)	Band gap (eV)	Ionization energy (eV/e-h pair)	Dielectric constant (ϵ_s/ϵ_0)
Si	14	2.33	1.12	3.61	11.9
SiC(4H)	14/6	3.21	3.23	7.8	9.66
Ge	32	5.33	0.68	2.98	16
GaAs	31/33	5.32	1.42	4.2	13.1
CdTe	48/52	6.06	1.52	4.43	10.36
$Cd_{0.9}Zn_{0.1}Te$ (CZT)	48/30/52	6.0	1.60	5.0	10.63
HgI_2	80/53	6.4	2.13	4.3	8.8
Semiconductor	Intrinsic resistivity (Ω-cm)	Electron mobility ($cm^2/V{\cdot}s$)	Hole mobility ($cm^2/V{\cdot}s$)	Electron lifetime (s)	Hole lifetime (s)
Si	$>5 \times 10^4$	1500	450	$>10^{-3}$	$>10^{-3}$
SiC	$>10^{15}$	900	120	4×10^{-7}	6.7×10^{-7}
Ge	47	3900	1900	$>10^{-3}$	$>10^{-3}$
GaAs	$\approx 10^8$	>8000	400	10^{-9}–10^{-8}	10^{-9}–10^{-8}
CdTe	10^9	1050	100	3×10^{-6}	2×10^{-6}
CZT	10^{11}	1350	120	10^{-6}	5×10^{-8}
HgI_2	10^{13}	100	4	$>10^{-6}$	$>10^{-6}$

where N_s is the doping concentration of the *lighter* doped side. Note that qV_{bi} is equal to the conduction band energy difference from the p-type side to the n-type side (see Fig. 4), where

$$V_{bi} \approx \frac{kT}{q} \ln\left(\frac{N_D N_A}{{n_i}^2}\right). \tag{14}$$

At room temperature, the material resistivity can be expressed as

$$\rho_s = \frac{1}{q\mu_s N_s}, \tag{15}$$

where N_s and μ_s are the background dopant concentration and mobility for the lighter doped side of the junction, and Eq. (13) can be rewritten as

$$W \approx \{2\epsilon_s \mu_s \rho_s (V_{bi} - V)\}^{1/2}. \tag{16}$$

The electric field magnitude across the device is

$$|\mathrm{E}(x)| \approx \frac{qN_s}{\epsilon_s}(W - x), \quad 0 \le x \le W. \tag{17}$$

The active radiation-sensitive volume of the *pn* junction detector is defined by the space charge region (or depletion region), and the undepleted regions act as series resistances. Detectors based on *pn* junction diodes are typically operated under *reverse bias*, which is regarded as a negative voltage but is actually a positive voltage applied to the *n*-type material with respect to the *p*-type material. Shown in Fig. 5 is the band diagram of a reverse-biased *pn* junction. The large energy band barriers prevent electrons on the *n*-type side from diffusing over to the *p*-type side and prevent holes on the *p*-type side from diffusing into the *n*-type side. As a result, the junction suppresses leakage current that would be present if the semiconductor were operated as a resistor. This necessary condition reduces the electron current such that small charge packets excited in the depletion region by radiation interactions can be measured.

There are some sources of leakage current, as depicted in Fig. 5. Although the *majority* carriers on the *p*-type side are holes, according to Eq. (4), a small concentration of electrons is still present. These *minority* charge carriers (electrons) can diffuse into the depletion region, where they are swept across by the electric field and contribute to the leakage current. A similar case is true for holes diffusing from the *n*-type side into the depletion region. Leakage current can also occur from thermal generation of electrons directly across the band gap into the conduction band, producing electron and hole free carriers. Thermal generation of such charge carriers can be suppressed by cooling the detector while it is operating. Under high voltage bias conditions, charge carriers can also tunnel directly across the band gap, again contributing to the leakage current. Variations about the leakage current can be a significant source of electronic noise (shot noise), which decreases the overall energy resolution of the detector. Basically, *pn* junctions are employed to minimize leakage currents in semiconductor detectors.

The capacitance of a parallel contact *pn* junction detector is given by

$$C_{\text{det}} = \frac{\epsilon_s A}{W}, \tag{18}$$

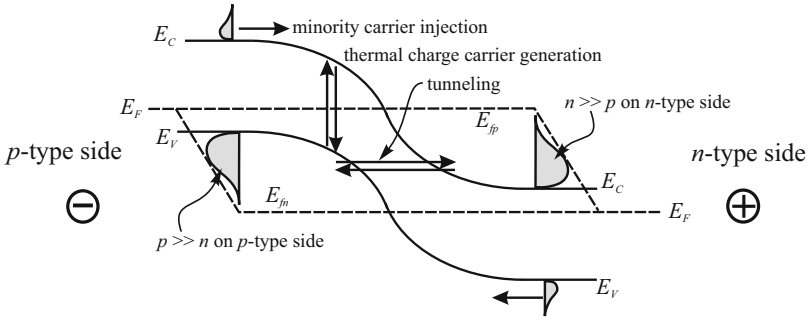

Fig. 5 In reverse bias, the density of available carriers, dominated by the *minority* carrier concentration, determines the leakage current. At higher voltages, bulk generation and tunneling may increase the observed leakage currents.

where A is the device active contact area. Substituting Eq. (16) into Eq. (18),

$$C_{\text{det}} \approx A \left[\frac{\epsilon_s}{2\mu_s \rho_s (V_{bi} - V)} \right]^{1/2}. \tag{19}$$

Detector capacitance affects the input voltage pulse height, with a large capacitance diminishing the input voltage from the detector that is measured by the amplification circuit, as

$$V_{\text{in}} \approx \frac{Q}{C_{\text{tot}}}, \tag{20}$$

where C_{tot} is the total capacitance (detector and coupling) and Q is the total charge collected from the radiation detector after a radiation event. Hence, it is important to reduce detector capacitance and coupling capacitance between the detector and the shaping electronics. From Eq. (19), it is seen that increasing the reverse bias voltage decreases the detector capacitance but at the expense of increasing the leakage current.

pin Junction Devices

Reverse biased diode detectors need a sizeable depletion region to maximize efficient radiation absorption. As found in Eq. (13), the depletion region width is proportional to the square root of the applied reverse voltage, indicating that excessive voltage would be required to product a sizeable depletion region for a common *pn* junction diode. The usual remedy is to construct a *pin* diode, which has an intrinsic or high purity region, between the *p*-type and *n*-type contacts. The *p*- and *n*-type contacts can produce either blocking barriers or electrically *ohmic* contacts to the material. The application of *p*-type contacts to *p*-type material, or *n*-type contacts to *n*-type material, generally produces non-rectifying electrical contacts that follow Ohm's law.

The device may have a truly intrinsic region between the *p*- and *n*-type contacts, in which the electron and hole populations are identical, or the high purity region may be a lightly doped material. Lightly doped *p*-type material is commonly denoted π-type, and lightly doped *n*-type material is commonly denoted ν-type. Analysis of the diode construction should take into account the "punch-through" voltage, in which the depletion region extends completely across the high purity region, whether the material is i, ν, or π type. Semiconductor pin diode radiation detectors are commonly operated at biases above the punch-through voltage.

Intrinsic material either has dopant concentrations below the intrinsic concentration or has compensation dopants that cause the residual free carrier concentration to be below the intrinsic concentration. In either case, the residual space charge is practically zero ($\rho_c \approx 0$), and from Eq. (11), the resulting electric field is constant across the pin diode under reverse bias. Many detectors are fashioned from high

purity semiconductor materials, yet these actually are not intrinsic behaving, having some residual dopant concentration that is still above the intrinsic concentration. As a result, ρ_c is nonzero, although small, and the depletion region width is determined by V_{bi} and the applied voltage. If the lightly doped π or ν regions are relatively thin, the detector might be "fully depleted" without an applied voltage, as depicted in Fig. 6. Usually, such is not the case, and a reverse bias must be applied to extend the depletion region and electric field across the device as determined from Eqs. (13) and (17), respectively.

Schottky Devices

The application of a metal to a semiconductor surface acts to bend the semiconductor bands to form an energy barrier $q\phi_{bn}$, much like the pn junction diode, as shown in Fig. 7. The Fermi energies, defined by the metal and semiconductor work functions (ϕ_m and ϕ_s), must align when the two materials are brought into contact (Henisch 1984). Because the semiconductor work function changes with doping concentration, reference is usually made to the semiconductor electron affinity ($q\chi_s$), the difference between the vacuum level at full ionization and the conduction band edge. As a result of the junction formation, a built-in potential $q\phi_{bi}$ forms, and potential barrier $q\phi_{bn}$ forms (Sharma 1984; Rhoderick and Williams 1988). Under a reverse bias, this energy barrier serves to reduce leakage current. Typically the barrier height is lower than that for pn or pin junction diodes; hence detectors based on the Schottky barrier diode typically have higher leakage currents than pn or pin diodes. Because the surfaces of semiconductors have defects, interface states, and possible contaminants, the actual barrier height not only depends upon the choice of

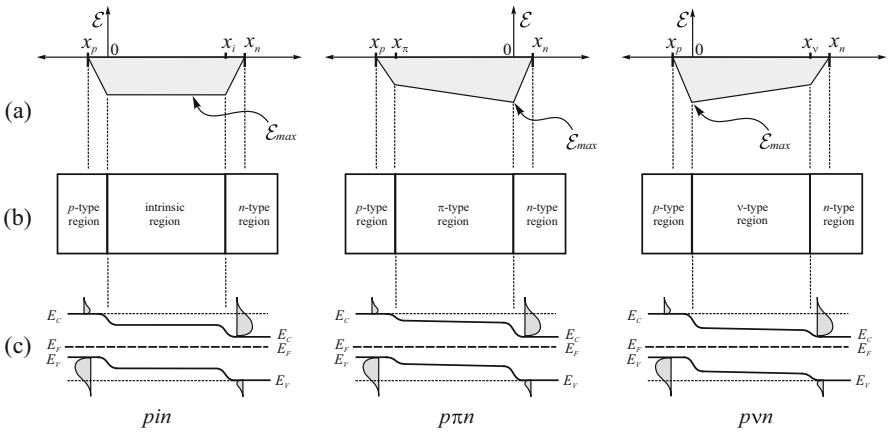

Fig. 6 Electric field (**a**) and band diagrams (**c**) of pin, $p\pi n$, and $p\nu n$ devices. Note that the electric field across the intrinsic region of the pin diode is constant, but the lightly doped $p\pi n$ and $p\nu n$ have a definite slope to their electric fields

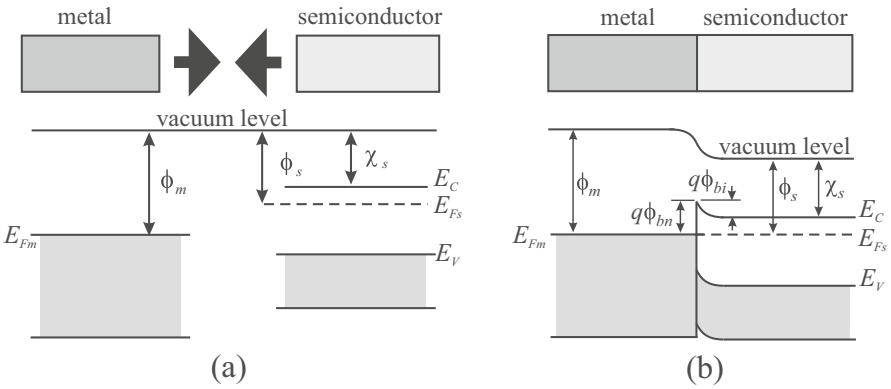

Fig. 7 The band configuration depicted for a metal and semiconductor (**a**) before and (**b**) after contact, according to the Schottky-Mott model

metal but also on how the surface is prepared. These surface states can effectively "pin" the detector barrier height, thereby predetermining the actual value of $q\phi_{bn}$ before the metal is applied. The depletion width for a Schottky barrier detector is similar to a one-sided *pn* junction diode:

$$W \approx \left\{ \frac{2\epsilon_s (V_{bi} - V)}{q N_s} \right\}^{1/2}, \tag{21}$$

where N_s is the dopant concentration in the semiconductor. Just as Eq. (13) can be rewritten as Eq. (16), Eq. (21) can be rewritten as

$$W \approx \{2\epsilon_s \mu_s \rho_s (V_{bi} - V)\}^{1/2}. \tag{22}$$

The value of V_{bi} for common Schottky diodes is 0.3 volts. Note that Schottky contacts can be formed on *n*-type or *p*-type semiconductors, as depicted in Fig. 8. Besides being simple to construct, Schottky barrier detectors have a thin entrance region at the contact, unlike most *pn* and *pin* diodes, and energy attenuation in this "dead region" is kept to a minimum. As a result, Schottky barrier detectors (sometimes called "surface barrier detectors") are attractive as charged particle spectrometers.

Ohmic Contacts

Efficient charge carrier extraction from a semiconductor detector requires ohmic behaving contacts; hence, it is important in some cases that the metal/semiconductor interface does *not* form a rectifying potential barrier. For instance, metal contacts to the *n* and *p* regions of *pn* and *pin* detectors are processed to be non-rectifying,

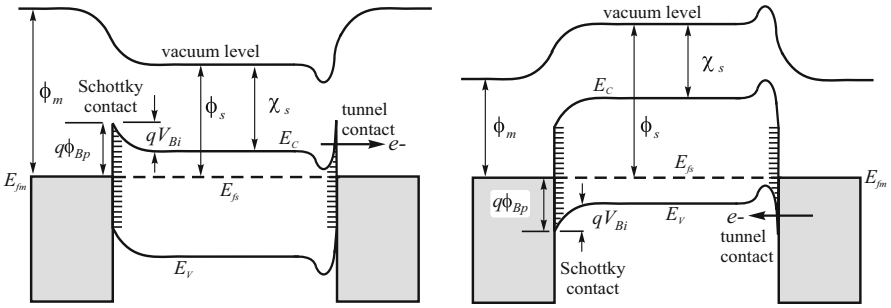

Fig. 8 Interface states alter the interface potentials and effectively "pin" the Schottky barrier. Shown are *n*-type and *p*-type Schottky barriers, along with *n*-type and *p*-type tunneling ohmic contacts

or *ohmic*, and generally follow Ohm's law. Unfortunately, due to interface state pinning, a barrier is formed for almost all metals applied to a semiconductor surface. To remedy this problem, a high concentration of dopants is applied with the metal and diffused, typically through thermal treatment, into the semiconductor (Schwartz 1969). The process causes the Schottky barrier to become extremely thin so that electrons can tunnel directly through the barrier; hence the contact has ohmic behavior. Schottky diodes are typically constructed with one (or more) Schottky contact as a rectifying barrier to reduce leakage current and one (or more) opposing ohmic contact to allow for efficient carrier extraction, thereby reducing electronic noise (see depiction in Fig. 8).

Resistive Devices

Semiconductor detectors fabricated from wide band gap materials (generally >1.6 eV) have material resistivities high enough to reduce leakage currents to low levels and as a result do not require rectifying contacts to suppress leakage currents. The devices typically have ohmic contacts for electrodes to prevent rectification and the subsequent formation of space charge regions (which can limit the active region volume). Radiation interactions in the detectors excite electron-hole pairs that are swept out of the detectors by an applied electric field. The high resistivity of the device insures that the leakage current is lower than the radiation-excited current. For example, the current from a common 5 mm (width) $\times$ 10 mm $\times$ 10 mm CdZnTe detector of band gap 1.62 eV has a resistivity of 10^{11} Ω cm, giving a detector resistance of 5×10^{10} Ω. A bias of 600 volts would produce a 12 nA leakage current. With average excitation energy w of 5 eV per electron-hole pair, a 662 keV gamma-ray will excite approximately 2×10^{-14} C. With a charge sweep out time across the detector of 320 ns, the integrated background charge is 3.8×10^{-15} C, only 19% of the charge excited by the gamma-ray.

Photoconductive Devices

There is a unique class of semiconductor detectors known as photoconductors. In principle, such devices are composed of semiconducting material upon which ohmic contacts have been applied to prevent the formation of a blocking barrier or a space charge region. From Eq. (7), the resistivity of a semiconductor material is inversely proportional to the free carrier concentration. A single radiation absorption event will cause the local conductivity to change spontaneously, yet the small charge cloud is surrounded by higher resistivity material on all sides. Further, the charge cloud is dissipated rapidly by an applied voltage.

Suppose instead the semiconductor block is saturated with a radiation pulse such that electron-hole pairs are evenly distributed throughout the crystal bulk. The conductivity of the entire semiconductor block changes because of the macroscopic change in the free carrier concentration. This means that, for any constant applied voltage, the current through the device must increase. The current continues to flow, with well-fabricated ohmic contacts, since Ohm's law dictates that every electron exiting the device at the anode is replaced by another electron injected at the cathode. This *photocurrent* continues to flow, decaying away as a function of the charge carrier lifetimes. Hence, the photocurrent is described as

$$I(t) = \left(\frac{VA}{W}\right) q \left[\mu_e (n + n_{ph} e^{-t/\tau_e}) + \mu_h (p + p_{ph} e^{-t/\tau_h})\right], \tag{23}$$

where n_{ph} and p_{ph} are the excess free carrier concentrations excited by the radiation pulse and n and p are the steady-state free carrier concentrations just before the radiation pulse is produced.

This result is important. First, the current decays away as a function of the free-charge-carrier lifetimes, so that the current continues to flow even after the primary charge carriers excited in the semiconductor reach the electrodes. Second, the duration of the detector current pulse can be tailored by changing the free-charge-carrier lifetimes. High-speed photoconductive radiation detectors can be manufactured by purposely adding lifetime shortening dopants or by shortening the lifetimes with intentional radiation damage. These detectors have been used for fast-timing measurements of radiation bursts.

Operation

Semiconductor detectors operate on the principle of induced charge, in which mobile charges drifting through the detector cause charge to flow in an externally connected circuit, typically a preamplifier for pulse-mode operation. This concept is important, mainly because the detector produces voltage pulses that depend on the RC time constant of the output circuit, the capacitance of the detector, the coupling capacitance, and the charge-carrier velocities. Further, the voltage pulse induced by the detector begins to form *immediately* when the charges begin to

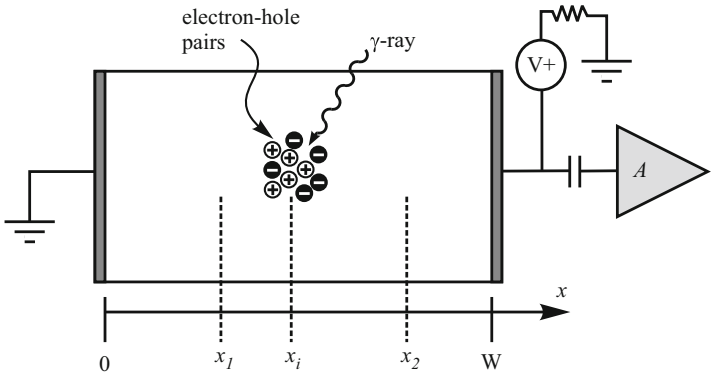

Fig. 9 Planar semiconductor detector configuration

move in the detector. From Fig. 9, N_0 electron-hole pairs excited at point x_i in a detector with active region of width W will induce a current according to the scaled motion of electrons and holes. The total liberated charge of the electron-hole pairs is represented by $Q = qN_0$.

Consider a semiconductor detector with n number of electrodes where mobile charges are in motion within the device. The induced current on the ith electrode among a set of two or more electrodes is (Shockley 1938)

$$i_i = \frac{dQ_i}{dt} = -\frac{Q}{V_i}\nabla V(\mathbf{r}) \cdot \frac{d\mathbf{r}}{dt} = \frac{Q}{V_i}\mathrm{E}(\mathbf{r}) \cdot \mathbf{v}, \tag{24}$$

where Q_i is the image charge on electrode i, $\mathbf{v}$ is the charge-carrier velocity, $\mathrm{E}(\mathbf{r})$ is the electric field at point $\mathbf{r}$ under the condition that the "potential" at electrode i is set at V_i with all other electrodes grounded, and $V(\mathbf{r})$ is the potential at location $\mathbf{r}$ within the system. It is useful to normalize $V(\mathbf{r})$ by setting V_i to one volt, i.e., define $V_w(\mathbf{r}) = V(\mathbf{r})/V_i$. This normalized "potential" V_w is called the *weighting potential* although it is dimensionless. In terms of this normalized potential, Eq. (24) is expressed as

$$i_i = -Q\nabla V_w(\mathbf{r}) \cdot \frac{d\mathbf{r}}{dt} = Q\mathrm{E}_w(\mathbf{r}) \cdot \mathbf{v} \tag{25}$$

and

$$Q_i = -QV_w(\mathbf{r}) \tag{26}$$

where the normalized or weighting electric field is $\mathrm{E}_w = \mathrm{E}/V_i = -\nabla V_w$. This result can be applied to any one of the electrodes by setting its potential to one volt and grounding all other electrodes (set to zero); see also Jen (1941) and Beck (1953). The results of Eq. (25) are significant and important and are often referred

to as *Ramo's Theorem* (Although Eq. (25) is commonly called Ramo's theorem, the same result was published by Shockley in 1938 a year before Ramo's publication in 1939, and it is a straightforward derivation from Green's theorem. Also, because both V_w and E_w are dimensionless, Eq. (25) is dimensionally correct, although some forget this fact). Hence, for any geometric detector structure, the expected current induction for the electrode tied to the readout circuit can be found with Eq. (25). The weighting potential for a simple planar detector is

$$V_w|_{\text{planar}} = \frac{x}{W} \tag{27}$$

which is clearly a linear function of position in the detector. Hence, the current induced is directly proportional to the distance charge carriers travel across the detector width W within time t. Suppose electron-hole pairs are created at position x_i and the holes are drifted to position x_1 while electrons are drifted to position x_2. Using Eq. (27), the solution from Eq. (24) yields the total change in the induced charge from the motion of electrons and holes:

$$\Delta Q|_{\text{planar}} = Q\left[\frac{x_i - x_1}{W}\bigg|_h + \frac{x_2 - x_i}{W}\bigg|_e\right] = Q\left[\frac{x_2 - x_1}{W}\right]. \tag{28}$$

From Fig. 9 and Eq. (28), it becomes clear that if the holes and electrons reach their respective electrodes, where $x_2 - x_1 = W$, the change in the induced charge ΔQ is the same as Q, a case referred to as *complete charge collection*. Any condition in which the electrons and/or holes do not completely reach their respective electrodes results in incomplete charge collection, and $\Delta Q < Q$.

The induced current is not a linear function of position for detector configurations other than planar devices. Other basic detector configurations include coaxial designs and spherical (hemispherical) designs (see Fig. 10). It can be shown that the weighting potential for a cylindrical detector is

$$V_w|_{\text{cylinder}} = \ln\left(\frac{r}{r_2}\right)\left[\ln\left(\frac{r_1}{r_2}\right)\right]^{-1}, \tag{29}$$

where r_2 is the detector outer radius and r_1 is the detector inner radius. The weighting potentials for various r_1/r_2 cases are shown in Fig. 11. With this result, the solution to Eq. (24) for a coaxial detector configuration is

$$\Delta Q|_{\text{cylinder}} = Q\left[\ln\left(\frac{r_2}{r_1}\right)\right]^{-1} \ln\left(\frac{r_2'}{r_1'}\right), \tag{30}$$

where r_1' and r_2' are the drift radii locations for the electrons and holes. Note that the weighting potential is not linear for the cylindrical case and a larger change in the weighting potential is apparent in the vicinity near the inner electrode at r_1,

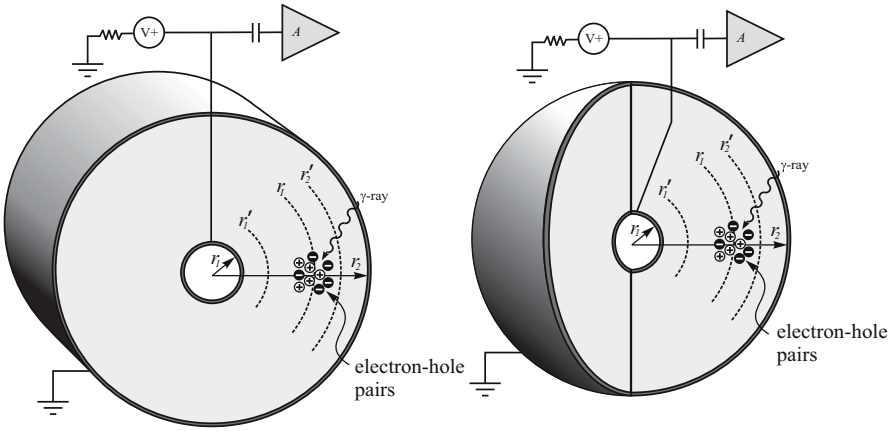

Fig. 10 Cylindrical and spherical semiconductor detector configurations

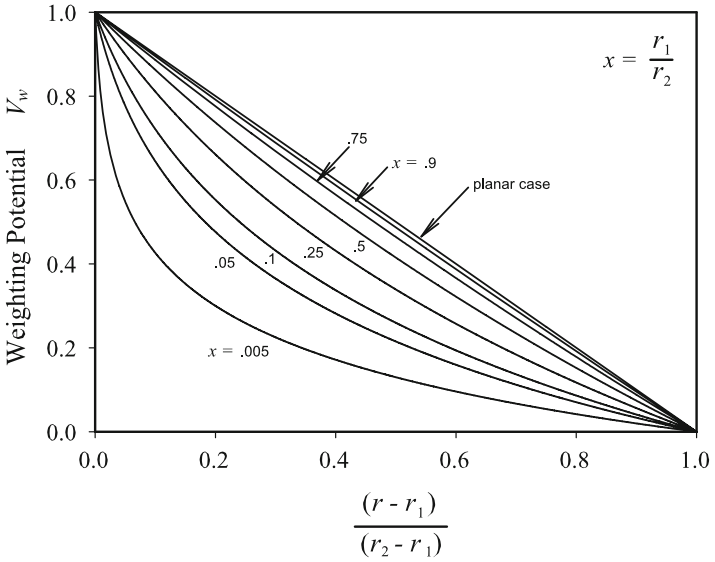

Fig. 11 Weighting potentials for various values of r_1/r_2 versus the normalized distance from r_1 to r_2 for a cylindrical detector

and therefore the induced current is much higher for charges moving near the inner electrode than for charges moving near the outer electrode at r_2.

Similarly, it can also be shown that the weighting potential for a spherical (or hemispherical) detector is

$$V_w|_{\text{sphere}} = \left(\frac{r_1}{r_2 - r_1}\right)\left(\frac{r_2}{r} - 1\right), \tag{31}$$

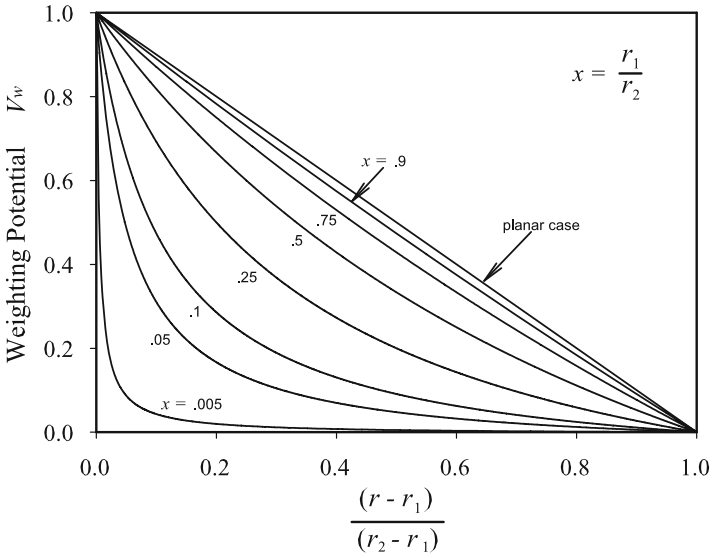

Fig. 12 Weighting potentials for various values of r_1/r_2 versus the normalized distance from r_1 to r_2 for a spherical detector

where r_2 is the detector outer radius and r_1 is the detector inner radius. The weighting potentials for various r_1/r_2 cases are shown in Fig. 12. The solution to Eq. (24) for a hemispherical detector is

$$\Delta Q|_{\text{sphere}} = Q\frac{r_1 r_2}{r_1' r_2'}\left[\frac{r_1' - r_2'}{r_1 - r_2}\right], \tag{32}$$

where r_1' and r_2' are the drift radii locations for the electrons and holes. Note again that the weighting potential is not linear for the spherical case and a larger change in the weighting potential is apparent near the inner electrode at r_1. The induced current is much higher for charges moving near the inner electrode than for charges moving near the outer electrode at r_2. The weighting potential in detectors with complex geometric shapes can be found by solving Eq. (24) through numerical methods.

Because the capacitance of a detector is highly dependent upon the bias voltage, mainly because the size of the depleted active region changes with bias voltage, it is important that the preamplifier circuit used to sense the induced current is properly matched to the detector. Further, the preamplifier should be a *charge-sensitive* preamplifier, in which the pulse height output is largely insensitive to capacitance changes in the semiconductor detector and is instead mainly dependent upon the charge collected from the detector. Commercial detectors generally have specifications with recommended preamplifier characteristics that can serve to optimize the detector performance.

Gamma-Ray and X-Ray Spectrometers

Properties sought for an ideal γ-ray spectrometer include a wide band gap energy, high Z material composition, high atomic density, long charge carrier lifetimes, high resistivity, high electron and hole mobilities, and a small ionization energy. A wide band gap energy (>1.5 eV) and high resistivity allow room temperature operation that otherwise would require cryogenic cooling to reduce electronic noise. High atomic density and high Z components increase the γ-ray interaction probability (see Fig. 13). Long charge carrier lifetimes and high carrier mobilities increase the charge collection efficiency and produce better spectroscopic results. Finally, a small ionization energy causes increased numbers of excited charge carriers, thereby improving statistics and enhancing spectroscopic energy resolution. Unfortunately, no existing semiconductor actually has all of these characteristics; hence the investigator should select a semiconductor detector best suited for the desired application. The basic properties of several semiconductors used for γ-ray and x-ray detectors are listed in Table 2.

X-ray Detectors Based Upon Si

Si is a group IV elemental semiconductor with a room temperature band gap energy of 1.12 eV. Its low Z number and low density of electrons cause its γ-ray absorption

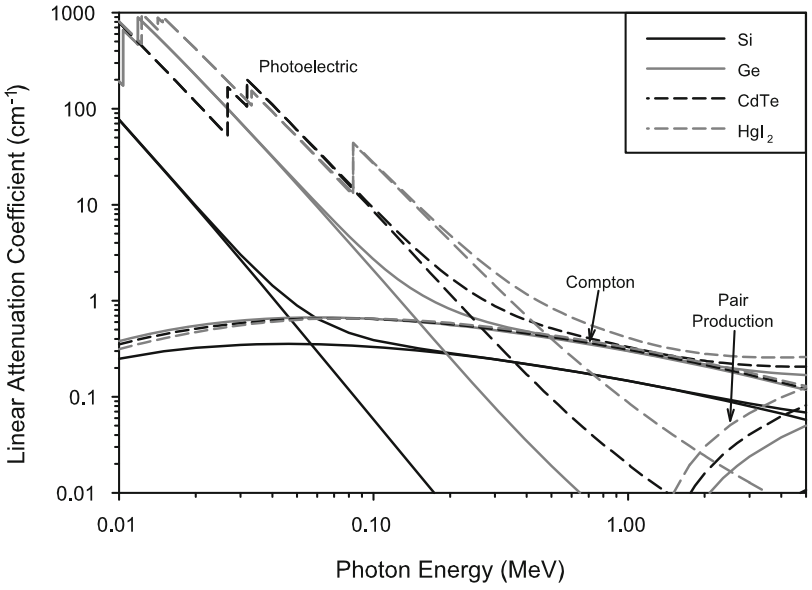

Fig. 13 Photon linear attenuation coefficients as a function of photon energy for Si, Ge, CdTe, and HgI_2 semiconductor materials

coefficient to be small. Further, the energy at which the photoelectric effect equals the Compton scattering effect is relatively low at only 60 keV. Hence, Si is a poor choice for high-energy γ-ray spectroscopy. However, its K absorption edge appears at 1.838 keV, meaning that the absorption edge discontinuity does not adversely affect x-ray absorption at higher energies nor does the appearance of x-ray escape peaks cause significant issues in spectra. By comparison, the K absorption edge for Ge is 11.103 keV. The fact that higher-energy γ-rays have less chance of interacting in Si serves to reduce the background effects. Energy resolution is quoted in terms of energy spread at the full width at half the maximum (FWHM) of a spectral full energy peak. Silicon detectors deliver excellent energy resolution, with a FWHM of

$$FWHM = \left[(FWHM_{\text{noise}})^2 + \left(2.35\sqrt{wFE} \right)^2 \right]^{1/2}, \tag{33}$$

where w is the average energy to produce an electron-hole pair, E is the photon energy, and F is the Fano factor (typically 0.1). The Fano factor is a correction factor to account for typically higher-energy resolution than predicted from pure Gaussian statistics. For these reasons, Si does have importance as an x-ray spectrometer for applications such as x-ray fluorescence, x-ray microanalysis, particle-induced x-ray emission (PIXE), x-ray absorption spectroscopy (XAS), x-ray diffraction, and Mössbauer spectroscopy at energies generally below 50 keV.

Basic Design

Highly purified Si can be fashioned into a type of *pin* diode; yet from Eq. (12), these devices are limited to depleted regions less than 2-mm width, an unsatisfactory thickness for efficient x-ray absorption. The problem is remedied by compensating the remaining impurities in Si with the Li-drifting technique, in which Li ions are electrically introduced deep into the semiconductor under controlled conditions. The resulting devices, denoted as Si(Li) detectors, have active regions ranging from 3 to 5 mm. The basic design is shown in Fig. 14. Although Si(Li) detectors can be operated at room temperature, they perform best when cooled to low temperatures. Various Si(Li) detectors are available coupled to either liquid nitrogen (LN2) dewars or Peltier coolers.

The detectors are encapsulated in a protective container with a thin entrance window, typically constructed from Be. The entrance window of the detector affects the low-energy sensitivity limit. Shown in Fig. 15 is the detection efficiency for various Si(Li) detectors with different thicknesses and different entrance windows. Note that thicker detectors increase the efficiency for higher-energy x-rays, while the appropriate choice of entrance window can increase the efficiency for low-energy x-rays. An example x-ray spectrum from a fluoresced brass sample taken with a Si(Li) detector is shown in Fig. 16.

Si(Li) detectors can be commercially acquired in a variety of segmented patterns, including strips, triangular, and square patterns. The detectors consist of *pin* diode structures individually fabricated into a single Si substrate, thereby reducing "dead

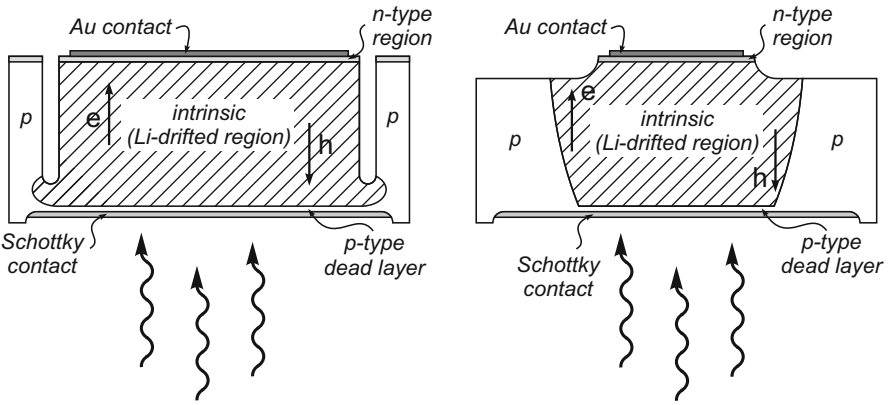

Fig. 14 Popular configurations for Si(Li) detectors, showing (left) the inverted T and (right) the etched planar. Copyright (2020). From Radiation Detection: Concepts, Methods and Devices by D. S. McGregor and J. K. Shultis. Reproduced by permission of Taylor and Francis Group, LLC, a division of Informa PLC.

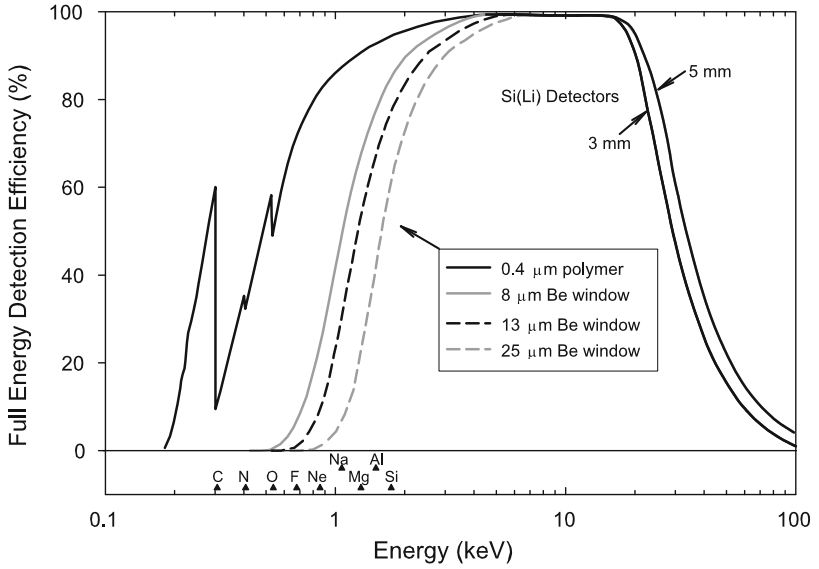

Fig. 15 The absorption efficiency of a Si(Li) detector as a function of x-ray energy, depletion thickness, and entrance window. (Data from Canberra 2003)

zones" between neighboring detectors. These detectors offer high x-ray energy resolution and spatial interaction information. Further, clever designs can actually improve count rate efficiency for ion probe instrumentation, such as PIXE, by surrounding the target region with multiple detectors. Used in conjunction with

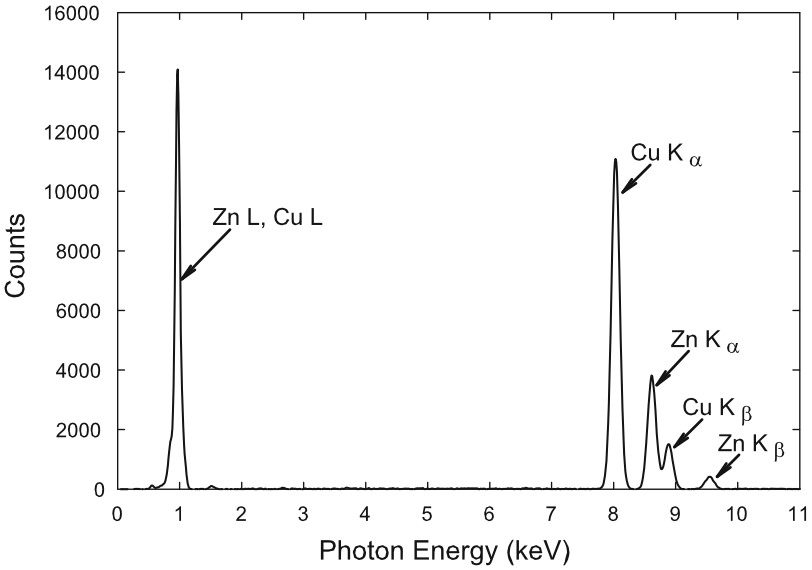

Fig. 16 X-ray spectrum of a brass sample taken with a Si(Li) detector. Copyright (2020). From Radiation Detection: Concepts, Methods and Devices by D. S. McGregor and J. K. Shultis. Reproduced by permission of Taylor and Francis Group, LLC, a division of Informa PLC.

other γ-ray detectors, the segmented Si(Li) detectors can be used for Compton scatter γ-ray cameras.

Detectors Based Upon Ge

Presently, the most popular high resolution γ-ray spectrometers are constructed from high purity Ge (HPGe). The material is purified through zone refinement, resulting in a nearly intrinsic material. Although numerous detector configurations exist (see Fig. 17), including special order devices, a standard unit is a coaxial $p\pi n$ or $p\nu n$ design with the rectifying junction on the outer surface. The coaxial design permits large detectors to be fabricated while minimizing the detector capacitance. With the rectifying surface on the outer surface, rather than on the inner surface, the active volume is increased, and the low-energy γ-ray detection efficiency is improved.

One difficulty with HPGe detector operation is the need to chill the device while operating. Because of the small band gap energy (0.68 eV), the intrinsic carrier concentration of electrons and holes is much too high at room temperature, and significant leakage current is produced when operated at high voltage, which can damage the detector. For this reason, HPGe detectors are typically attached to a dewar and cooled with LN2, or they are attached to a low noise refrigerator system. To ensure that the damage does not occur from excessive leakage current should the

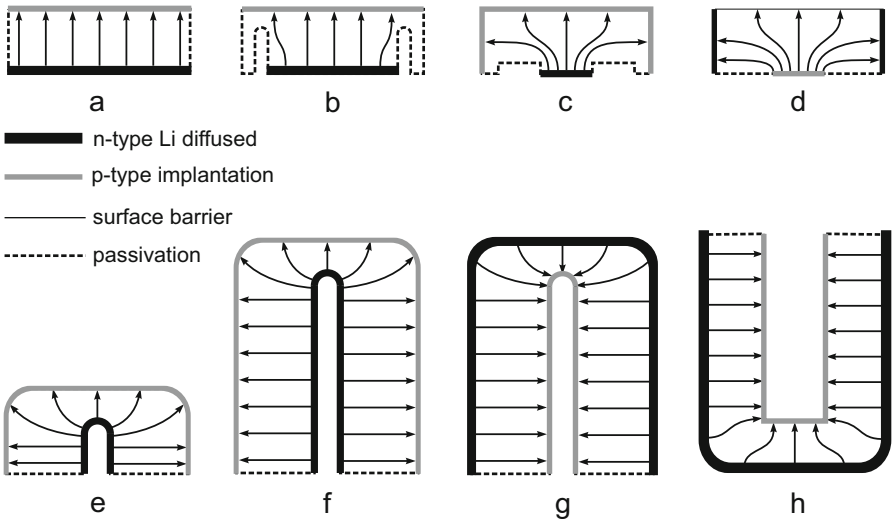

Fig. 17 Different commercially available HPGe detector structures with electric field lines depicted: (**a**) basic planar detector, (**b**) grooved planar, (**c**) low capacitance planar, (**d**) surface barrier planar, (**e**) truncated $p\nu n$ blind coaxial, (**f**) $p\nu n$ blind coaxial, (**g**) $n\pi p$ blind coaxial, and (**h**) $p\pi n$ well configuration. (After Darken and Cox 1995, Canberra 2016 and Ortec 2016)

LN2 be exhausted, most modern systems have a safety shutoff that disconnects the high voltage if the HPGe detector increases to a preset temperature. Portable survey detectors and laboratory units are available with either LN2 dewars or electrically cooled refrigerators. Hybrid LN2/electrical cryostats have become available, where the main cooler is electrical, backed up with LN2 cooling in case of a power outage.

The usual standard for quality comparisons of HPGe detectors is to quote the energy resolution for 1.33 MeV γ-rays from ^{60}Co. The expected energy resolution can be approximated by Eq. (33), where the Fano factor is approximately 0.08. Efficiency, for historical reasons, is quoted most often as a comparison to a 3 in $\times$ 3 in (7.62 $\times$ 7.62 cm) right cylindrical NaI(Tl) detector with the source placed 25 cm from the face of either detector. For instance, a relative 30% HPGe detector has 30% of the efficiency expected from a 3 in $\times$ 3 in NaI(Tl) detector at 1.33 MeV. Although useful as an approximation of detector performance, due to differences in detector geometries and mounting apparatuses, such sweeping generalizations can be erroneous for accurate measurements. It is best to characterize the detector efficiency and resolution, a method described by ANSI/IEEE 325-1996. A calibrated National Institute of Standards ^{60}Co check source is placed 25 cm from the front of the detector face. The number of counts appearing in the full energy peak for the 1.332 MeV γ-ray is divided by the number of emissions over that same time interval, which yields the absolute efficiency. The relative efficiency is found by dividing the absolute efficiency by 1.2×10^{-3}, which is the standard efficiency for a 3 in $\times$ 3 in NaI(Tl) detector under the same irradiation conditions. Comparison

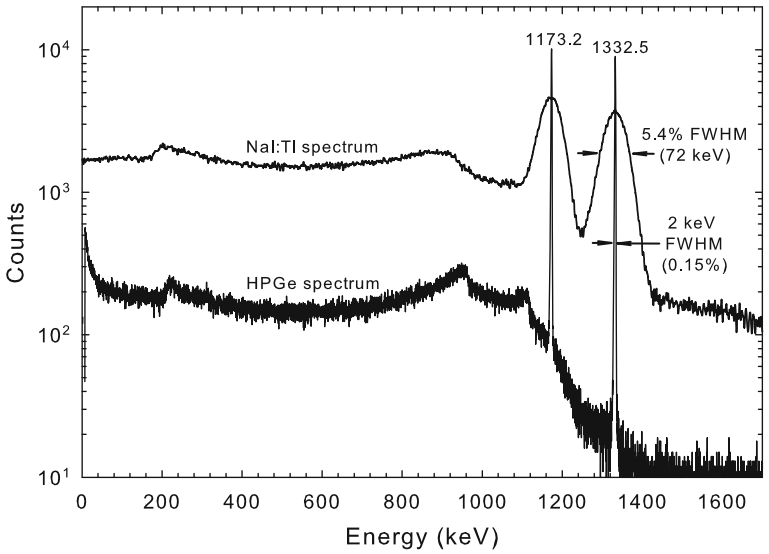

Fig. 18 Comparison gamma-ray spectra of ^{60}Co taken with a NaI(Tl) detector and a 20% relative efficiency HPGe detector. Copyright (2020). From Radiation Detection: Concepts, Methods and Devices by D. S. McGregor and J. K. Shultis. Reproduced by permission of Taylor and Francis Group, LLC, a division of Informa PLC.

spectra between a 20% relative efficiency HPGe detector and a 3×3 NaI(Tl) detector are shown in Fig. 18.

Various Designs

HPGe detectors are manufactured in various shapes, although most conform to either a planar or coaxial design. Small detectors are commonly manufactured as planar detectors. Relatively large HPGe detectors are manufactured as coaxial devices mainly to keep detector capacitance low. Small HPGe detectors usually have better energy resolution than larger devices, and the larger detectors have better γ-ray detection efficiency. The response functions for ν-type and π-type HPGe detectors are quite different at low energies.

High purity π-type detectors are fabricated with Li, an n-type dopant, traditionally diffused at a depth of approximately 700 μm thick around the outer surface. A much thinner implanted junction of p-type dopant (typically boron), approximately 300 nm deep, is formed as the ohmic contact. Consequently, the relatively thick "dead" layer formed by the outer contact significantly reduces the detector sensitivity to low-energy photons (typically below 40 keV). Some commercial units are now offered with thinner n-type contacts to reduce this dead layer. From Eqs. (29) and (30), the reverse bias configuration and geometry cause the average output pulse to be dominated by hole motion. These $n\pi p$ HPGe detectors

typically have slightly better energy resolution than *pvn* HPGe detectors at high γ-ray energies.

High purity ν-type detectors are fabricated with p-type dopants implanted and activated at a depth of approximately 300 nm for the outer rectifying contact. A much thicker diffused Li junction up to 700 μm thick is fabricated as the ohmic contact. As a result, low-energy γ-rays and x-rays encounter less "dead" layer in the outer contact, thereby increasing the efficiency for these low-energy photons. To take further advantage of the thin surface contact, these ν-type detectors are typically packaged in a can that has a thin Be window, thereby minimizing γ-ray and x-ray attenuation through the detector container. An additional advantage with ν-type HPGe detectors is their increased radiation hardness to neutron radiation. Neutron damage tends to form hole trapping sites; hence the electron-dominated pulses from ν-type HPGe detectors are somewhat less effected.

Examples of efficiency responses for a few HPGe variations are shown in Fig. 19. Notice in Fig. 19 the dip in efficiency at the Ge K absorption edge (11.1 keV). Also note the efficiency reduction below 100 keV for the π-type HPGe detector, which only becomes an issue for the ν-type devices represented in Fig. 19 at energies below

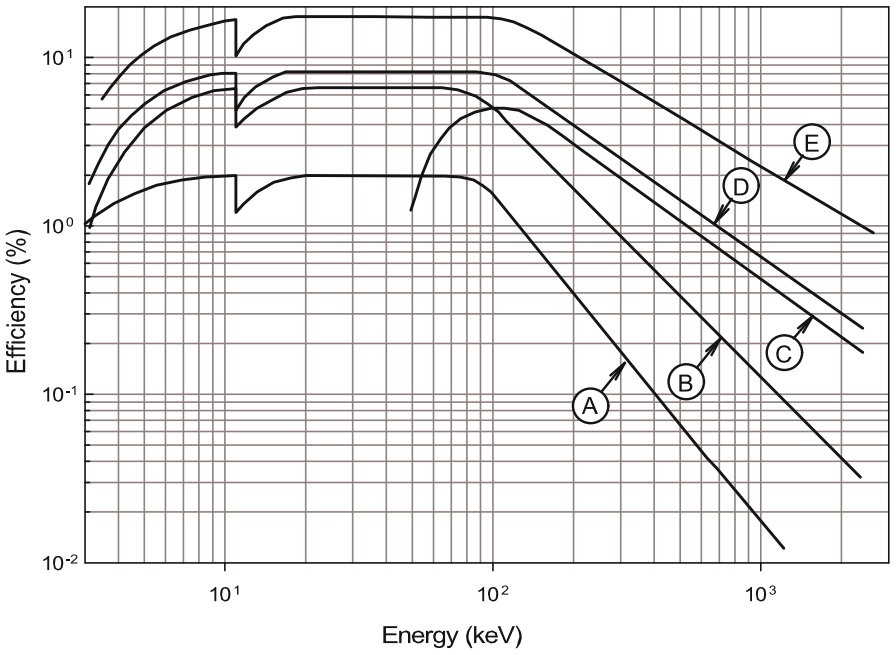

Fig. 19 The absolute detection efficiency for several HPGe detector configurations, showing a (A) 200 mm^2 × 10 mm thick low-energy ν-type nominally planar HPGe detector, (B) 10 cm^2 × 15 mm thick low-energy ν-type nominally planar HPGe detector, (C) coaxial π-type HPGe detector with 10% relative efficiency, (D) coaxial thin window ν-type 15% relative efficiency HPGe detector, and a (E) broad energy range π-type 5000 mm^2 × 30 mm thick nominally planar HPGe detector. (After Canberra 2016)

10 keV. The drop in efficiency is due to a combination of photon absorption in the detector contact dead region and the container holding the detector. Overall, the decision regarding which HPGe detector is best for an application requires some knowledge of the preferred energy resolution, necessary detection efficiency, and the photon energy range of interest (Table 3).

Compound Semiconductor Detectors

Compound semiconductor detectors have become more important in recent years, with commercial units now available. Typically these detectors are somewhat smaller than Si- and Ge-based detectors, mainly due to material imperfections (Schlesinger and James 1995). Regardless, a few materials, namely CdTe, CdZnTe, and HgI_2, have desirable properties for room-temperature-operated devices, an advantage not shared by Si(Li) or HPGe detectors. The reason for this advantageous property is their larger band gap energies that work to reduce their intrinsic carrier concentrations and substantially increase their resistivities at 300 K. Further, CdTe, CdZnTe, and HgI_2 all have relatively high Z atomic constituents and hence have larger gamma-ray absorption coefficients over those of Si and Ge. Still, because of their typical smaller size, energy resolution for these compound semiconductor detectors is usually reported relative to 662 keV gamma-rays of ^{137}Cs instead of 1.33 MeV gamma rays from ^{60}Co.

The total charge collected is usually affected by crystalline imperfections that serve as *trapping* sites, which are energy states that remove free charge carriers from the conduction and valence bands (Bertolini and Coche 1968). Charge is induced while these charge carriers are in motion; hence, their removal diminishes the output voltage. Although the actual trapping process is complicated, it is typical to describe the relative charge collection efficiency as a simplified function of trapping. For planar shaped detectors, this is induced charge given by

$$\frac{\Delta Q}{Q} = \xi_e(1 - \mathrm{e}^{-x/(\xi_e W)}) + \xi_h(1 - \mathrm{e}^{(x-W)/(\xi_h W)}), \tag{34}$$

where W is the detector active region width, Q is the initial excited charge magnitude, x is the event location in the detector, and

$$\xi_{e,h} = \left(\frac{\tau_{e,h} v_{e,h}}{W}\right) = \left(\frac{\mu_{e,h} \tau_{e,h} V}{W^2}\right), \tag{35}$$

where τ is the charge carrier lifetime, v is the charge carrier speed, and V is the applied operating voltage. Note that the relative charge collection is dependent upon the interaction location x and, for low values of ξ, the energy resolution is poor. Typically, good energy resolution is achieved if $\xi > 50$ for both electrons and holes, where $\Delta Q/Q$ has little deviation over the detector width W. Otherwise, the energy resolution suffers for higher-energy γ-rays (more or less >300 keV). The value of ξ

Table 3 Typically quoted energy resolution performance for some commercial semiconductor detectors

Detector	Area (mm^2)	Radiation type	Energy (keV)	FWHM (keV)	Comments	Source
Si(Li)	12.5	γ rays	5.9	0.155–0.175	LN2 cooled	M,O
Si(Li)	20	γ rays	5.9	0.180	Peltier cooled	B
		γ rays	59.6	0.450	Peltier cooled	
Si(Li)	28–30	γ rays	5.9	0.165–0.180	LN2 cooled	M,O
Si(Li)	80	γ rays	5.9	0.175–0.190	LN2 cooled	M,O
Si(Li)	200	γ rays	5.9	0.220	LN2 cooled	M,O
Si *pin*	13	γ rays	5.9	0.18–0.22	Peltier cooled	A
	25	γ rays	5.9	0.127–0.230	Peltier cooled	
CdTe	9	γ rays	122	$\leq$1.2	Peltier cooled	A
Schottky	25	γ rays	122	$\leq$1.5	Peltier cooled	
CdZnTe	$\approx$100	γ rays	122	$\leq$6.1	Room temp	K
hemisphere	$\approx$100	γ rays	662	$\leq$20	Room temp	B,K
CdZnTe	100	γ rays	662	13.2–26.4	Room temp	K
coplanar	225	γ rays	662	16.5–26.4	Room temp	
implanted	100	α particles	5486	13	W = 100 μm	M,O
Si diode			5486	12	W = 500 μm	
implanted	450	α particles	5486	17–21	W = 100 μm	M,O
Si diode			5486	15–19	W = 500 μm	
implanted	900	α particles	5486	27–33	W = 100 μm	M,O
Si diode			5486	22–28	W = 500 μm	
p-type	50	α particles	5486	15–17	W = 100 μm	O
SSB		α particles	5486	15–17	W = 500 μm	
p-type	150	α particles	5486	16–19	W = 100 μm	O
SSB		α particles	5486	16–18	W = 500 μm	
p-type	900	α particles	5486	30–40	W = 100 μm	O
SSB		α particles	5486	30–53	W = 500 μm	
HPGe detector	Relative eff. (%)	Radiation type	Energy (keV)	FWHM (keV)	Comments	Source
p-type	20	γ rays	122	0.715–0.975	LN2 or mech cooled	B,I,M,O
coaxial	50			0.9–1.2	LN2 or mech cooled	B,I,M,O
	100			1.2–1.4	LN2 or mech cooled	B,I,M,O
p-type	20	γ rays	1332	1.8–2.0	LN2 or mech cooled	B,I,M,O
coaxial	50			1.9–2.1	LN2 or mech cooled	B,I,M,O
	100			2.0–2.3	LN2 or mech cooled	B,I,M,O
n-type	20	γ rays	122	0.69–1.0	LN2 or mech cooled	I,M,O
coaxial	50			0.86–1.2	LN2 or mech cooled	I,M,O
	70			1.1–1.3	LN2 or mech cooled	I,M,O

(continued)

Table 3 (continued)

HPGe detector	Relative eff. (%)	Radiation type	Energy (keV)	FWHM (keV)	Comments	Source
n-type	20	γ rays	1332	1.8–2.0	LN2 or mech cooled	I,M,O
coaxial	50			2.1–2.3	LN2 or mech cooled	I,M,O
	70			2.3–2.5	LN2 or mech cooled	I,M,O

A AmpTek, *B* Baltic Scientific, *I* Itech, *K* Kromek, *M* Mirion, *O* Ortec (Ametek)
These detectors are only a few representative examples and do not account for the numerous variations available nor a complete list of detector sources. Contact vendors to acquire a full listing of detector sizes and performance statistics

can be increased by decreasing the detector size (W), increasing carrier lifetimes (τ) through material improvement, or increasing the applied voltage V. Due to practical voltage limitations and the fundamental difficulty with improving materials, most compound semiconductor detectors are manufactured with small active widths to improve detector energy resolution, and hence, the devices are relatively small. The $\mu\tau$ values for electrons and holes are often quoted measures of quality for compound semiconductors used as γ-ray spectrometers.

Methods of overcoming the charge carrier trapping problem have been introduced that use electronic correction methods, novel electrode and structural designs to optimize the weighting potentials, or a combination of both. Examples of these *single carrier designs* include quasi-hemispherical designs, coplanar electrode designs, small pixel effect designs, Frisch effect designs (Frisch collar, Frisch ring), and drift ring designs (McGregor and Shultis 2021; Owens 2019).

CdTe

Cadmium telluride (CdTe) is a wide band gap semiconductor of interest as a room-temperature-operated gamma-ray spectrometer. CdTe has a cubic zinc blende crystal structure and a room temperature direct band gap energy of about 1.52 eV. The average ionization energy is 4.43 eV per e-h pair with a 0.11 Fano factor. The dielectric constant ($\kappa = \epsilon_s/\epsilon_0$) for CdTe is 10.36 (Strauss 1977).

CdTe is relatively soft, rating 54 on the Knoop hardness scale (approximately 2.2 on Mohs scale). The elemental constituents have atomic numbers 48 and 52, and the density of CdTe is 5.86 g cm^{-3}. Because of the relatively high Z numbers, photoelectric absorption dominates up to approximately 260 keV. Charge carrier mobilities are 1050 cm^2 V^{-1} s^{-1} for electrons and 100 cm^2 V^{-1} s^{-1} for holes. Electron and hole mean free drift times are material dependent but often quoted near 3×10^{-6} s and 2×10^{-6} s, respectively.

The wide band gap should yield an intrinsic resistivity of 10^9 Ω cm. Although the band gap is wide enough for room temperature operation, because of background impurity contamination, resistivities greater than 10^9 Ω cm are difficult to achieve. As a result, leakage currents are too high to operate CdTe detectors as resistive devices. The detectors are manufactured as *pn* junction or Schottky junction diodes

to reduce leakage current to manageable levels. Further, high resistivity is usually achieved through impurity and defect compensation, typically with Cl.

Because of material imperfections, mainly impurities, charge carrier trapping compromises the energy resolution performance. Consequently, these devices continue to be manufactured as small detectors, and the detector volumes are usually no more than a few mm thick. Commercial units are available as small gamma-ray spectrometers. Typically, the best energy resolution is achieved with the assistance of small electronic Peltier coolers.

CdZnTe

The introduction of Zn in the growth process of CdTe, nominally between 2% and 15%, has led to the production of CdZnTe detectors (This particular semiconductor is denoted CZT (common), (Cd,Zn)Te (less common), $Cd_{1-x}Zn_xTe$, or CdZnTe. By adhering to traditional elemental symbols, and because of the many different elemental combinations in use for substrates and detectors, the author chooses to use CdZnTe.). Overall, CdZnTe detectors have the same advantages as CdTe detectors with several added benefits. By adding a small amount of ZnTe to the melt, many important semiconductor properties are drastically improved. The band gap of CdZnTe increases with Zn concentration, with band gap energy of $Cd_{1-x}Zn_xTe$ at 300 K is well approximated by (Olego et al. 1985)

$$E_g(x)\,\text{eV} = (1.51 \pm 0.005) + (0.606 \pm 0.01)x + (0.139 \pm 0.01)x^2\,\text{eV}. \quad (36)$$

The band gap ranges from 1.52 to 1.64 eV for Zn contents ranging from $x = 0.02$ to $x = 0.2$; hence the detectors can operate at room temperature without serious leakage current concerns. With an increased band gap energy, the intrinsic free carrier concentration diminishes, thereby increasing the resistivity while reducing detector leakage current. Butler et al. (1992) report that adding $x = 0.2$ amount of Zn changes the resistivity of CdTe from $3 \times 10^9\ \Omega\,\text{cm}$ to $2.5 \times 10^{11}\ \Omega\,\text{cm}$ for $Cd_{0.8}Zn_{0.2}Te$. The gamma-ray absorption efficiency of CdZnTe is similar to that of CdTe, with a slight decrease in absorption efficiency with increased concentrations of Zn ($Z = 30$). The dielectric constant is approximately 10.6 for CdZnTe, although this property is also a function of the Zn concentration. The addition of Zn increases the hardness of CdZnTe over CdTe and decreases the dislocation density (Anand 2013). The ionization energy is approximately 5 eV per e-h pair, although this number changes as a function of band gap energy. The Fano factor of CdZnTe has been measured to be approximately 0.11 (Bale et al. 1999) at 233 K, with at least one research group (Redus et al. 1997) reporting a lower Fano factor of 0.089 also at 233 K.

The etch pit density (EPD) is a measure of the dislocation defect density. Butler et al. (1993) show a marked reduction in the EPD as the Zn content was increased, with the densities of $1.5 \times 10^5\ \text{cm}^{-2}$, $10^4\ \text{cm}^{-2}$, and $5 \times 10^3\ \text{cm}^{-2}$ for Zn contents of 0, 0.04, and 0.2, respectively. Further, CdZnTe detectors do not exhibit the polarization phenomenon at low irradiation levels, which are often observed with CdTe detectors. However, Wang et al. (2013) report the observation of polarization

from CdZnTe detectors under high irradiation conditions. An additional benefit of incorporating Zn is that CdZnTe devices, because of the increased band gap and resistivity, can be operated at higher temperatures than CdTe devices, and they can also resolve lower-energy photon energies (x-rays and gamma-rays) traditionally difficult to observe with CdTe detectors.

Due to improved materials properties, they can be manufactured much larger than conventional CdTe detectors, and the detectors can operate at room temperature usually without leakage current problems. Because of the high resistivity, the detectors are typically manufactured with ohmic contacts for the cathodes and anodes and are operated as resistive detectors rather than junction diodes.

The detectors have adequate electron transport properties but poor hole transport properties. As a result, conventional planar detectors, similar to the depiction in Fig. 9, seldom produce useful energy resolution for moderate to high-energy γ-rays ($\geq$300 keV). Instead, some commercial manufacturers rely upon electronic correction methods, clever electrode contact shapes, and special geometric detector shapes to modify the weighting potential and electronic signal such that electrons dominate signal formation rather than holes (McGregor and Shultis 2021; Owens 2019). Energy resolution below 7 keV FWHM for 662 keV γ-rays can be achieved at room temperature for these single carrier detector designs. CdZnTe detectors are presently used in handheld γ-ray spectrometers, smaller medical imaging apparatuses, and advanced pixelated imaging devices.

HgI_2

Attractive for its large Z components, mercuric iodide (HgI_2) has long been studied as a gamma-ray spectrometer with varying degrees of success [see McGregor and Shultis 2021 and references therein]. HgI_2 has atomic numbers of 80 and 53 with a volume density of 6.4 g cm^{-3}. The α-phase (red) of HgI_2 has measured charge carrier mobilities of 100 cm^2 V^{-1} s^{-1} for electrons and 4 cm^2 V^{-1} s^{-1} for holes (Ponpon et al. 1975). Thus a substantial voltage is required to ensure acceptably high charge carrier collection. HgI_2 has a measured average ionization energy of 4.42 eV per e-h pair with a Fano factor of 0.19 (Ricker et al. 1982). Because of the large atomic number of mercury (80), the photoelectric effect is predominant for gamma-ray energies below 400 keV (see Fig. 13). As a result, HgI_2 detectors can be relatively thinner than other common semiconductors and still have comparable efficiencies. For example, the absorption efficiency for 140-keV gamma-rays in a 2-mm-thick HgI_2 detector is similar to 4.2-mm-thick CdTe or CdZnTe detectors and 1.9-cm-thick Ge or GaAs detectors (McGregor and Hermon 1997). The α-phase of HgI_2 has a band gap energy of 2.13 eV and has a resistivity of about 10^{13} Ω cm.

They have fewer commercial applications than CdTe or CdZnTe, mainly because of process and fabrication issues. HgI_2 is a layered tetragonal crystal structure (α phase) and is a soft material with a Knoop hardness less than 10 (below 1 on the Mohs scale). HgI_2 is also highly reactive, and only a few materials are known to be compatible for electrical contacts, those being carbon (Aquadag®), Pd, and Pt. HgI_2 detectors are usually encapsulated with parylene to prevent decomposition over time. The material is known to *polarize* over time, which is manifested as the gradual

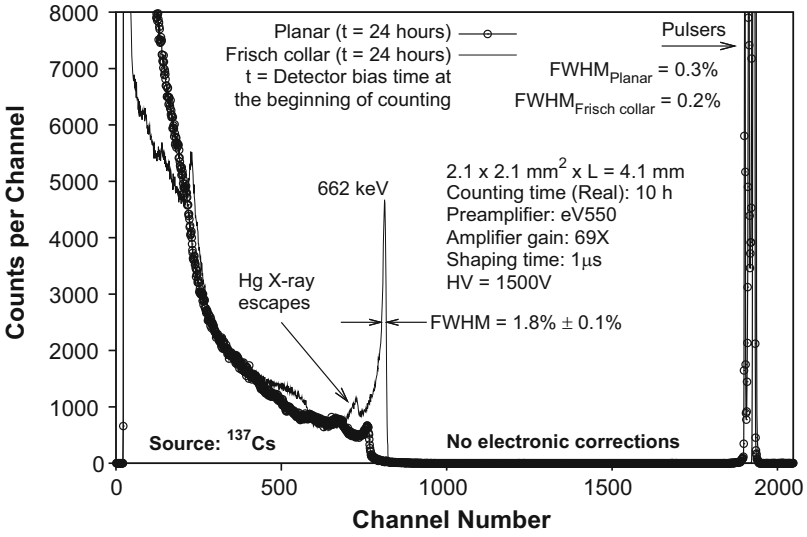

Fig. 20 Pulse height spectra taken with a 2.1 × 2.1 × 4.1 mm^3 HgI_2 device with and without a Frisch collar. A 1.8% FWHM energy resolution was measured with 662-keV gamma-rays from ^{137}Cs when using the Frisch collar. (From Ariesanti et al. (2010); copyright Elsevier (2010), reproduced with permission)

change in spectral features over time. Charge carrier loss from trapping is also a problem with HgI_2. Combined with the low charge carrier mobilities, HgI_2 detectors are usually kept volumetrically small to improve energy resolution. Single carrier detector designs such as pixelated electrode patterns and Frisch collar structures have been used to improve performance. Example spectra from a HgI_2 detector, with and without a Frisch collar structure, are shown in Fig. 20. The material has been used for portable x-ray spectrometers for in situ analysis, and modular units are available for specialized room temperature spectroscopy applications.

Charged Particle Detectors

Semiconductor charged particle spectrometers offer high-energy resolution for energetic ions. Typically, the devices are operated in vacuum, along with the source, to eliminate energy losses from a charged particle as its passes from the source to the detector. The detectors are typically designed with thin contacts and/or thin *pn* junctions in order to reduce particle energy loss in the nonsensitive (or dead) region of the contact. Because low Z elements have less problems with ion backscattering, Si is typically the material choice for particle detectors.

A simple nomogram representing the depletion width as a function of voltage and impurity concentration can be produced by linearizing Eq. (21) or Eq. (22) (Allcock et al. 1963; Blankenship and Borkowski 1960):

$$\log_{10}(W) = \frac{1}{2}\log_{10}\left[\left(\frac{2\epsilon_s}{q_e}\right)\left(\frac{V_{bi} - V}{N_b}\right)\right]$$

or

$$\log_{10}(W) - \frac{1}{2}\log_{10}(2\epsilon_s\mu) = \frac{1}{2}\left[\log_{10}(\rho) + \log_{10}(V_{bi} - V)\right], \tag{37}$$

where N_b has been replaced with $1/q_e\mu\rho$ and the applied voltage V is negative (reverse bias). With the properties for Si listed in Table 2, such a nomogram was developed for a silicon surface barrier detector, shown in Fig. 21, in which the depletion width is a function of material resistivity (n-type and p-type).

These detectors can be used for a variety of charged particle identification and characterization purposes, including high resolution spectroscopy of α particles, β particles, protons, and heavy ions, continuous air monitoring, and particle telescopes.

Surface Barrier and Implanted Junction Detectors

Si surface barrier (SSB) detectors rely upon the production of a thin Schottky barrier for a rectifying junction. A typical SSB detector cross section is shown in Fig. 22. High purity n-type or p-type Si is etched, mounted, and epoxied into a ceramic ring. Afterward, a thin layer of Au or Al, ranging from 80 to 200 nm, is applied to the semiconductor surfaces. The thin contact region minimizes the amount of energy lost by particles that enter the device, a necessary precaution to preserve high-energy resolution. However, these delicate surface barrier detectors can be easily damaged by improper handling and are often difficult to clean. Detectors can be obtained in a variety of sizes, ranging from a few mm to 50 mm diameter. These detectors are usually light sensitive and must be operated in darkness, although commercial companies do offer versions that can operate in ambient light, at the expense of energy resolution. Depletion depths range from approximately 100 microns up to, for special cases, 5 mm.

Implanted junction detectors rely upon an abrupt junction pn diode for rectification (see Fig. 22). These devices are commonly fabricated from high purity n-type Si. An oxide is grown on the devices for passivation, followed by etching windows back to the Si surface. Shallow p-type and n-type dopants are implanted on opposite sides of the Si surface and thermally activated (Martini 2017). This process produces dead layer junctions on the order of only 50 nm. Because there is no thin metallization layer over the detector, they are more robust and easier to clean than common SSB detectors. Implanted junction detectors can be used for the same basic detection functions that SSB detectors are used. An example alpha-particle spectrum taken with an implanted junction detection is shown in Fig. 23.

SSB and implanted junction detectors can be acquired in numerous shapes, sizes, and configurations, making them a versatile choice for particle detection

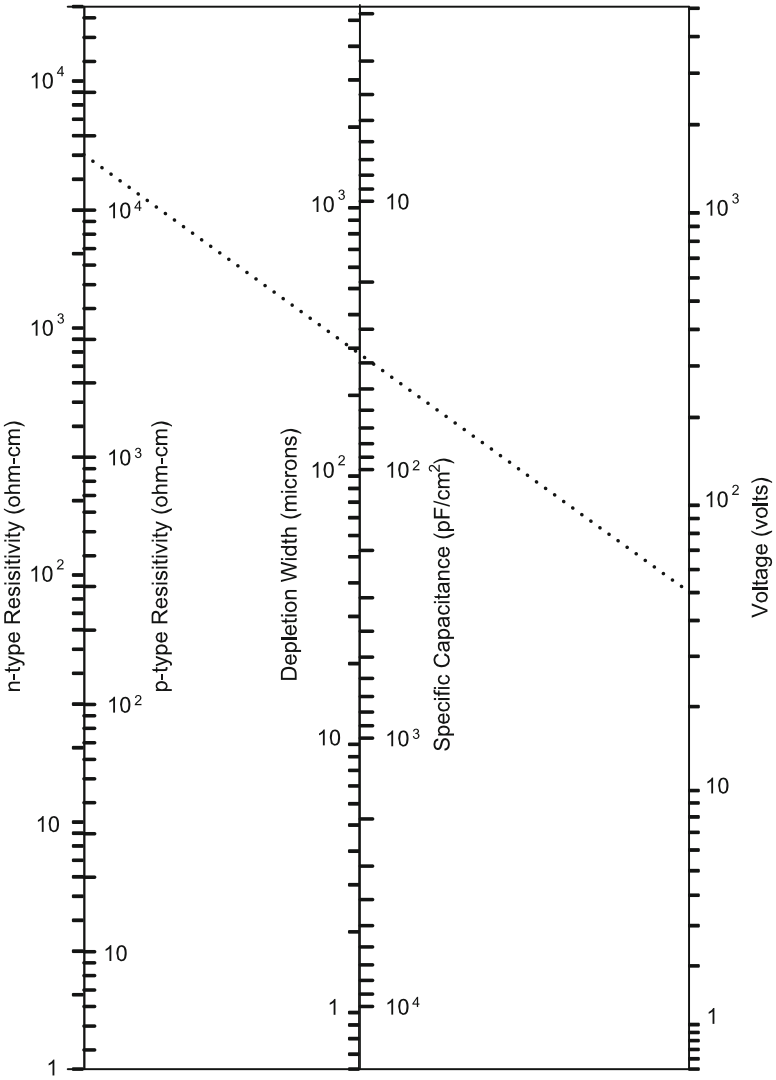

Fig. 21 The depletion region as a function of material resistivity and reverse voltage for Si particle detectors. A straight line will yield material resistivity (n or p type), the depletion depth, and applied voltage, according to Eq. (37). The example shown with the dotted line is for 5 kΩ n-type material at 50 volts reverse bias, which yields $W = 282$ microns. Copyright (2020). From Radiation Detection: Concepts, Methods and Devices by D. S. McGregor and J. K. Shultis. Reproduced by permission of Taylor and Francis Group, LLC, a division of Informa PLC.

and spectroscopy. Further, the detectors can be acquired as multielement arrays for position sensing and timing purposes. The adaptation of very large-scale integration (VLSI) processing technology to Si detectors allows for detector arrays to be

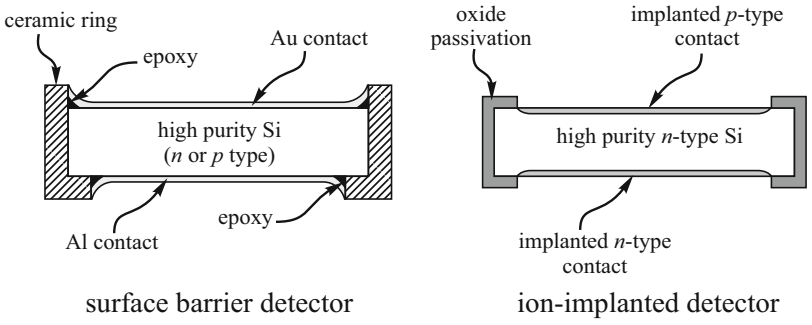

Fig. 22 General configurations for Si surface barrier detectors and implanted junction detectors

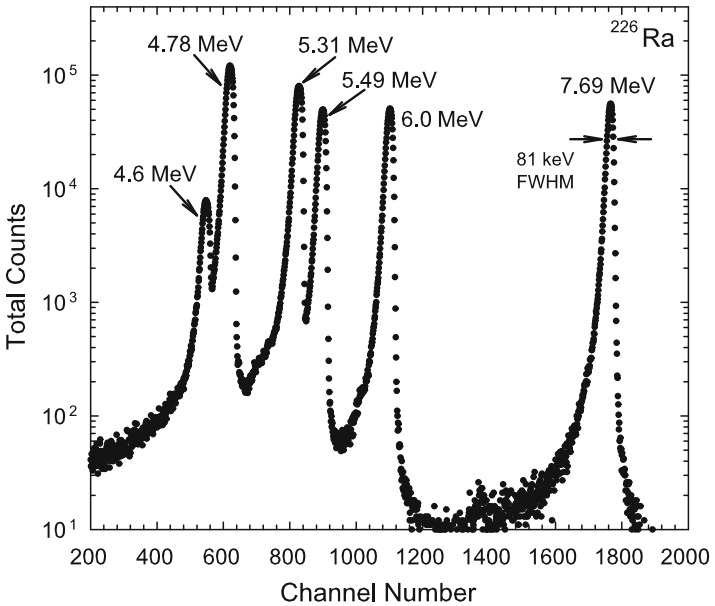

Fig. 23 Room temperature alpha-particle differential pulse-height spectrum of a spectroscopic grade ^{226}Ra source taken with a 24-mm diameter implanted junction Si detector operated in vacuum. Copyright (2020). From Radiation Detection: Concepts, Methods and Devices by D. S. McGregor and J. K. Shultis. Reproduced by permission of Taylor and Francis Group, LLC, a division of Informa PLC.

fabricated in a vast number of detector designs, including custom devices contracted to commercial vendors. The detectors are available as double-sided strip detectors with spatial resolutions as low as 25 μm and pad detectors with spatial resolution as small as 0.4 mm. Large arrays of position-sensitive Si detectors can be used in collider facilities, x-ray scattering, and Compton cameras. Finally, drift diode configurations, a variant design that drifts electronic charge carriers laterally along

the detector to a small collection contact, offer low capacitances with large sensitive areas (Gatti et al. 1985; Kemmer et al. 1987).

Neutron Detectors

Semiconductor radiation detectors used as neutron detectors are typically configured as *pn* junction or Schottky junction diodes coated with a neutron reactive material. The basic construction of such a detector is shown in Fig. 24, where a Schottky or *pn* junction diode detector has a coating of neutron reactive material applied to the surface. Typically the devices have either ^{10}B or ^{6}LiF as the active coating. The absorption cross sections for both ^{10}B and ^{6}Li follow a $1/v$ dependence. The ^{10}B(n,α)^{7}Li neutron reaction yields two possible de-excitation branches from the excited ^{11}B compound nucleus, namely:

$$
{}^{1}_{0}\mathrm{n} + {}^{10}_{5}\mathrm{B} \longrightarrow \begin{cases} {}^{4}_{2}\mathrm{He}\ (1.4721\ \mathrm{MeV}) + {}^{7}_{3}\mathrm{Li}^{*}\ (0.8398\ \mathrm{MeV}) & (93.7\%) \\ {}^{4}_{2}\mathrm{He}\ (1.7762\ \mathrm{MeV}) + {}^{7}_{3}\mathrm{Li}\ (1.0133\ \mathrm{MeV}) & (6.3\%), \end{cases}
$$

where the Li ion in the 94% branch is ejected in an excited state, which deexcites through the emission of a 480 keV gamma-ray. Fully enriched ^{10}B has a microscopic absorption cross section for thermal neutrons of 3840 barns. With a mass density of 2.15 g cm^{-3}, the solid structure of ^{10}B has a macroscopic thermal absorption cross section of 500 cm^{-1}.

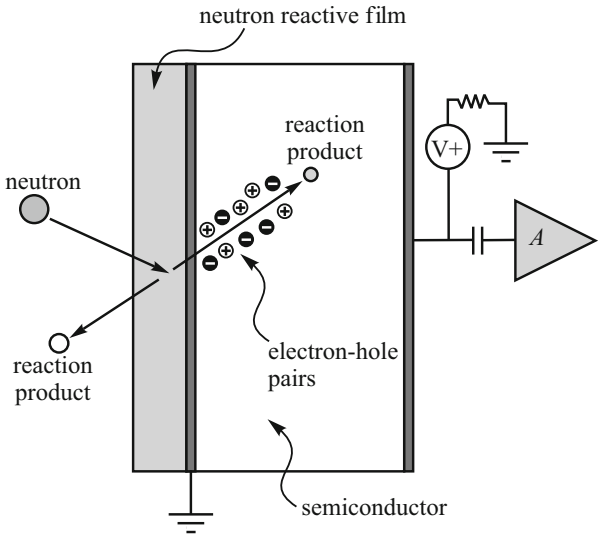

Fig. 24 Cross section of a coated semiconductor neutron detector

The ^{6}Li(n,t)^{4}He neutron reaction yields a single product branch:

$$^{1}_{0}\mathrm{n} + ^{6}_{3}\mathrm{Li} \longrightarrow ^{3}_{1}\mathrm{H}\,(2.7276\ \mathrm{MeV}) + ^{4}_{2}\mathrm{He}\,(2.0553\ \mathrm{MeV}).$$

The reaction products from the ^{6}Li(n,t)^{4}He reaction are more energetic than those of the ^{10}B(n,α)^{7}Li reaction and, hence, are much easier to detect and discriminate from background radiations. ^{6}Li has a relatively large microscopic thermal neutron absorption cross section of 940 b, although it is less than that of ^{10}B. Unfortunately, Li is a chemically reactive metal, and therefore, it is the stable compound ^{6}LiF, with a macroscopic cross section of 57.51 cm^{-1}, that is used as the reactive coating.

For thermal neutrons, the charged particle reaction products are ejected in opposite directions, meaning that only one reaction product can actually enter the semiconductor detector. Further, the reaction products lose energy as they pass through the neutron absorber to the semiconductor detector, thereby limiting the effective absorber thickness. Detectors of this type are limited to less than 5% thermal neutron detection efficiency (McGregor et al. 2003). These devices are generally not commercially available as independent units; rather they are sold as an active component inside some electronic dosimeter modules.

The low efficiency of coated planar diodes led to the development of microstructured semiconductor neutron detectors (MSNDs). These detectors have microscopic structures etched into a semiconductor substrate, subsequently formed into a *pin* style diode. The microstructures are backfilled with neutron reactive material, usually ^{6}LiF, although ^{10}B has also been used (see Fig. 25). The increased semiconductor surface area adjacent to the reactive material and the increased probability that a reaction product will enter the semiconductor greatly increase the intrinsic neutron detection efficiency. Commercial MSNDs backfilled with ^{6}LiF have quoted thermal neutron detection efficiencies between 30% and 35% with an average operating voltage of 3 volts. Advanced experimental versions of double-sided MSNDs with opposing microstructures on both sides of a semiconductor wafer have been reported with over 69% thermal neutron detection efficiency (Ochs et al. 2020).

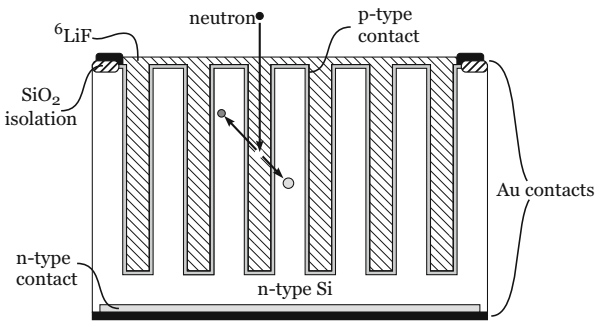

Fig. 25 The basic structure of an MSND

Summary

Semiconductor materials are attractive as radiation detectors for at least two main reasons. First, due to their low average ionization energy w, semiconductors produce a large number of signal charge carriers per unit energy, thereby decreasing statistical fluctuations beyond that of gas-filled and scintillation detectors, hence producing much better energy resolution. Second, semiconductor materials have energy band structures that allow their electrical properties to be altered through the addition of impurities. These materials can be manipulated to have a majority of negative (n-type) electrical charge carriers, or electrons, or positive (p-type) charge carriers, denoted "holes." Adjacent n-type and p-type materials can be manipulated to form detectors with rectifying contacts, which work to reduce both leakage current and electrical noise.

Semiconductor detectors can be fashioned into various detectors especially designed for x-ray detection, γ-detection, or charged particle detection. Detector performance is optimized by semiconductor choice and device design. Charged particle detectors are generally designed with low Z material, such as Si, to reduce backscattering. Higher Z materials, due to improved absorption efficiency, are generally used for γ-ray detectors. Low-energy x-ray and γ-ray detectors are often fabricated from Li-drifted Si (Si(Li) detectors), although the most commonly used semiconductor for photon detection is high purity Ge (HPGe detectors). Both Si(Li) and HPGe detectors must be cooled to low temperature for best operation. Wide band gap semiconductors, such as CdZnTe, can be used as room-temperature-operated γ-ray spectrometers.

Finally, semiconductor materials can be fashioned into arrays to yield spatial interaction information. These arrays can be arranged from the tiling of numerous individual detectors, or they can be fabricated as pixels upon a single semiconductor substrate. Commercial vendors offer numerous varieties of semiconductor detectors, which include particle, x-ray, and γ-ray detectors, in the form of individual devices or as arrays.

Cross-References

▸ Gamma-Ray Spectroscopy
▸ New Solid State Detectors
▸ Photon Detectors

References

Allcock HJ, Jones JR, Michel JGL (1963) The nomogram, 5th edn. Pitman, London

Anand KG (2013) Defects in Cadmium Zinc Telluride (CdZnTe) – a review. Int J Eng Manag Sci 4:113–120

Ariesanti E, Kargar A, McGregor DS (2010) Fabrication and spectroscopy results of mercuric iodide Frisch collar detectors. Nucl Instrum Meth A624:656–661

Bale G, Holland A, Seller P, Lowe B (1999) Cooled CdZnTe detectors for x-ray astronomy. Nucl Instrum Methods A436:150–154
Beck AHW (1953) Thermionic valves. Cambridge University Press, London
Bertolini G, Coche A (1968) Semiconductor detectors. Wiley, New York
Blankenship JL, Borkowski CJ (1960) Silicon surface barrier nuclear particle detectors. IRE Trans Nucl Sci NS-7:190–195
Butler JF, Lingren CL, Doty FP (1992) $Cd_{1-x}Zn_xTe$ gamma ray detectors. IEEE Trans Nucl Sci 39:605–609
Butler JF, Doty FP, Apotovsky B, Lajzerowicz J, Verger L (1993) Gamma- and x-ray detectors manufactured from $Cd_{1-x}Zn_xTe$ grown by a high pressure bridgman method. Mater Sci Eng B16:291–295
Canberra (2003) Silicon (Li) detector systems. Canberra Industries, Inc., Document CSP0157
Canberra (2016) Germanium detectors. Canberra Industries, Inc., Document C39606
Darken LS, Cox CE (1995) High-purity germanium detectors. In: Schlesinger TE, James RB (eds) Semiconductors for room temperature nuclear detector applications, Chapter 2. Part of the semiconductor and semimetals series, vol 43. Academic, San Diego, pp 23–83
Gatti E, Rehak P, Longoni A, Kemmer J, Holl P, Klanner R, Lutz G, Wylie A, Goulding F, Luke PN, Madden NW, Walton J (1985) Semiconductor Drift Chambers. IEEE Trans Nucl Sci NS-32:1204–1208
Henisch HK (1984) Semiconductor contacts; an approach to ideas and models. Clarendon Press, Oxford
Jen JK (1941) On the induced current and energy balance in electronics. Proc IRE 29:345–349
Kemmer J, Lutz G, Belau E, Prechtel U, Welser W (1987) Low capacity drift diode. Nucl Instrum Meth A253:378–381
Martini M (2017) Introduction to charged particle detectors, ORTEC Technical Note, Oak Ridge
McGregor DS, Hermon H (1997) Room-temperature compound semiconductor radiation detectors. Nucl Instrum Methods A395:101–124
McGregor DS, Shultis JK (2021) Radiation detection: concepts, methods, and devices. CRC Press, Boca Raton
McGregor DS, Hammig MD, Gersch HK, Yang Y-H, Klann RT (2003) Design considerations for thin film coated semiconductor thermal neutron detectors. Nucl Instrum Methods A500:272–308
McGregor DS, McNeil WJ, Bellinger SL, Unruh TC, Shultis JK (2009) Microstructured Semiconductor Neutron Detectors. Nucl Instrum Methods A608:125–131
Ochs TR, Bellinger SL, Fronk RG, Henson LC, Hutchins RM, McGregor DS (2020) Improved manufacturing and performance of the dual-sided microstructured semiconductor neutron detector (DS-MSND). Nucl Instrum Methods A954:paper 161696
Olego DJ, Faurie JP, Sivananthan S, Raccah PM (1985) Optoelectronic properties of $Cd_{1-x}Zn_xTe$ films grown by molecular beam epitaxy on GaAs substrates. Appl Phys Lett 47:1172–1174
Ortec (2016) PROFILE HPGe photon detector product configuration guide. Ametek, Document 012517
Owens A (2019) Semiconductor radiation detectors. CRC Press, Boca Raton
Pierret RF (1989) Advanced semiconductor fundamentals. Addison Wesley, Reading
Ponpon JP, Stuck R, Siffert P, Meyer B, Schwab C (1975) Properties of vapour phase grown mercuric iodide single crystal detectors. IEEE Trans Nucl Sci 22:182–191
Ramo S (1939) Current induced by electron motion. Proc IRE 27:584–585
Redus R, Pantazis J, Huber A, Jordanov V, Butler J, Apotovsky B (1997) Fano factor determination for CZT. Proc MRS 487:101–107
Rhoderick EH, Williams RH (1988) Metal-semiconductor contacts, 2nd edn. Clarendon Press, Oxford
Ricker GR, Vallerga JV, Dabrowski AJ, Iwanczyk JS, Entine G (1982) New measurement of the fano factor of mercuric iodide. Rev Sci Instrum 53:700–701
Schlesinger TE, James RB (1995) Semiconductors for room temperature nuclear detector applications. In: Semiconductors and semimetals, vol 43. Academic Press, San Diego

Schwartz B (1969) Ohmic contacts to semiconductors. Electrochemical Society, New York
Sharma BL (1984) Metal-semiconductor schottky barrier junctions and their applications. Plenum Press, New York
Shockley W (1938) Currents to conductors induced by a moving point charge. J Appl Phys 9:635–636
Strauss AJ (1977) The physical properties of cadmium telluride (1977) Revue de Physique Appliquee 12:167–184
Sze SM (1981) Physics of semiconductor devices, 2nd edn. Wiley, New York
Wang X, Xiao S, Li M, Zhang L, Cao Y, Chen Y (2013) Further process of polarization within a pixellated CdZnTe detector under intense x-ray irradiation. Nucl Instrum Methods A700:75–80

Further Reading

Dearnaley G, Northrop DC (1966) Semiconductor counters for nuclear radiations, 2nd edn. Wiley, New York
Deme S (1971) Semiconductor detectors for nuclear radiation measurement. Wiley, New York
Hannay NB (1959) Semiconductors. Reinhold, New York
Knoll GF (2010) Radiation detection and measurement, 4th edn. Wiley, New York
Lutz G (1999) Semiconductor radiation detectors. Springer, Berlin
Martini M, Ottaviani G (1969) Ramo's theorem and the energy balance equations in evaluating the current pulse from semiconductor detectors. Nucl Instrum Methods 67:177–178
McKelvey JP (1966) Solid state and semiconductor physics. Academic Press, New York
Nussbaum A (1962) Semiconductor device physics. Prentice Hall, Englewood Cliffs
Owens A (2012) Compound semiconductor radiation detectors. CRC Press, Boca Raton
Poenaru DN, Vîlcov N (1969) Measurement of nuclear radiations with semiconductor detectors. Chemical Pub, New York
Taylor JM (1963) Semiconductor particle detectors. Butterworth, London

Semiconductor Radiation Detector Suppliers

AmpTek-Ametek; www.amptek.com
Baltic Scientific Instruments; bsi.lv/en/
Eurorad; www.eurorad.com/detectors.php
Itech Instruments; www.itech-instruments.com/
Kromek; www.kromek.com/
Mirion Technologies; www.canberra.com/cbns/
Moxtek; www.moxtek.com/
Ortec-Ametek; www.ortec-online.com/
Radiation Detection Technologies, Inc.; www.radectech.com/
Radiation Monitoring Devices; dynasil.com/rmd
Redlen Technologies; www.redlen.com/